https://doi.org/10.5194/egusphere-2026-1289
Preprint. Discussion started: 21 May 2026

Century-long kilometre-scale Ocean eddy-rich global climate simulation with the coupled IFS CY48R1-FESOM 2.5 model

Rohit Ghosh[1], Suvarchal Kumar Cheedela[1], Sebastian Beyer[1], Nikolay Koldunov[1], Stella Berzina[2], Audrey Delpech[3], Svetlana Loza[1], Chathurika Wikramage[4], Stephy Libera[5], Matthias Aengenheyster[6], Amal John[1], Armelle Remedio[1], Patrick Scholz[1], Dmitry Sidorenko[1], Jan Streffing[1], Fabian Wachsmann[4], Thomas Jung[1,7]

[1]Alfred Wegener Institute Helmholtz Center for Polar and Marine Research (AWI), Bremerhaven, Germany
[2]ETH Zurich, Zurich, Switzerland
[3]Laboratoire d'Océanographie Physique et Spatiale, CNRS, Ifremer, IRD, University of Brest, Plouzané, France
[4]German Climate Computing Center (DKRZ), Hamburg, Germany
[5]Earth and Life Institute, Université Catholique de Louvain, Louvain-la-Neuve, Belgium
[6]European Centre for Medium Range Weather Forecasting (ECMWF), Reading, UK, Bonn, Germany
[7]Department of Physics and Electrical Engineering, University of Bremen, Bremen, Germany

Correspondence to: Rohit Ghosh (rohit.ghosh@awi.de)

Abstract

We present novel centennial-scale global climate simulations at kilometre-scale resolution utilizing the coupled IFS-FESOM model, featuring a 9 km atmosphere and a minimal 5 km ocean. Following the HighResMIP protocol, a 50-year high-resolution coupled spin-up was conducted, which was followed by a 65-year historical simulation (1950–2014) and a scenario simulation (SSP2-4.5, 2015-2050). This was accompanied by a 100-year control simulation (1950–2050) employing the 1950 radiative forcing. These simulations explicitly resolve ocean mesoscale eddies within a long-term climate context. Overall, the model demonstrates an improved mean climate state compared to CMIP6 models, with a notable reduction in persistent model biases, except for the polar regions. Performance metrics reveal reduced global errors in surface temperature, winds, and cloud formations. The very high-resolution ocean captures eddy-rich dynamics and realistic boundary current variability, contributing to an improved sea surface salinity patterns and a strengthened Atlantic Meridional Overturning Circulation (peak ~20 Sv). The simulation also reproduces internal climate variability with high fidelity, notably a realistic El Niño–Southern Oscillation with the desired quasi-periodicity (~4-5 years) and realistic winter teleconnection patterns. Sea ice and high-latitude biases have been identified as the primary remaining challenges: the model overestimates the extent of Arctic sea ice, resulting in a cold bias in the Northern high latitudes, while an initialization error in Antarctic snow cover induces a warm bias over Antarctica. Furthermore, there is a warm bias over the Weddell Sea with high ocean mix layer depth, associated with a winter devoid of sea ice. Despite persistent sea-ice and high-latitude biases, the coupled

https://doi.org/10.5194/egusphere-2026-1289
Preprint. Discussion started: 21 May 2026

system remains stable over centennial time scales with minimal long-term drift. These results demonstrate the feasibility and scientific value of global coupled climate simulations operating in the ocean eddy-rich regime at sub-10 km resolution. The IFS–FESOM kilometre-scale configuration thus represents a significant step forward in the development of next-generation Earth system models that robustly bridge global climate dynamics and regional-scale processes over multi-decadal to centennial periods.

1. Introduction:

Climate modeling has undergone significant advancements in recent decades, driven by improved scientific understanding and increased computational capabilities (Roberts et al., 2024; Schär et al., 2020). The development of high-resolution global climate models represents one crucial pathway, aiming to enhance the representation of critical processes and reduce persistent biases in climate simulations (Bordoni et al., 2025; Haarsma et al., 2016). Traditionally, state-of-the-art global climate models have operated at spatial resolutions of 50–100 km, necessitating the extensive use of parameterizations for many important small-scale processes. However, the advent of a more powerful high-performance computing systems has enabled climate simulations at resolutions where critical phenomena, such as ocean mesoscale eddies, can be explicitly resolved (Roberts et al., 2024).

The High Resolution Model Intercomparison Project phase 1 (HighResMIP) represents a coordinated effort to understand the effect of higher resolution (Haarsma et al., 2016; Roberts et al., 2024; Streffing et al., 2022). They performed systematic investigations of climate model resolution impacts by increasing atmospheric resolution from approximately 100–200 km to 25–50 km and ocean resolution from ~1° (eddy-parametrized) to ~0.25° (eddy-permitting), representing a significant advancement over typical CMIP6 resolutions of ~150 km atmosphere and 1° ocean. HighResMIP demonstrated substantial improvements in simulating key climate phenomena, including better representation of tropical cyclone intensity distributions and structure (Roberts et al., 2020a; Vannière et al., 2020), enhanced simulation of Gulf Stream separation (Roberts et al., 2019) and North Atlantic Current positioning (Moreno-Chamarro et al., 2021), improved Atlantic Ocean heat transports (Roberts et al., 2020b), more realistic precipitation distributions over complex topography (Demory et al., 2020). However, systematic analysis of HighResMIP results revealed that four major long-standing biases persisted even after these resolution increases: the warm eastern tropical oceans bias, the double Intertropical Convergence Zone (ITCZ), the warm Southern Ocean bias, and the cold North Atlantic bias (Moreno-Chamarro et al., 2022). In addition to these large-scale biases, significant coastal biases in air and sea surface temperatures were also unravelled and quantified (Delpech et al., 2025). These persistent biases, along with continued

https://doi.org/10.5194/egusphere-2026-1289
Preprint. Discussion started: 21 May 2026

large errors in tropical precipitation and cloud cover and modest improvements in midlatitude zonal winds, led to the conclusion that "further improved model physics, tuning, and even finer resolutions might be necessary" (Moreno-Chamarro et al., 2022).

Emerging evidence from eddy-rich ocean simulations (≤1/12° or ~8 km resolution) and km-scale atmospheric models (≤10 km) suggests significant potential for further improvements, with eddy-rich models demonstrating enhanced capability to capture observed sea surface temperature trends that standard CMIP6 models cannot reproduce (Chang et al., 2020; Yeager et al., 2023), representation of Gulf Stream separation that can be corrected at eddy-rich resolutions (Chassignet et al., 2020; Grist et al., 2021), and better simulation of Eastern Boundary Upwelling Systems through enhanced coastal upwelling and temperature gradients (Small et al., 2024). These developments indicate that the transition to eddy-rich ocean and km-scale atmospheric resolutions may represent a critical threshold for addressing some of the prominent, persistent biases that have limited climate model fidelity across multiple model generations.

A central factor underlying these advancements is the ability to explicitly resolve ocean mesoscale eddies. The importance of resolving these eddies cannot be overstated, as they play a crucial role in ocean dynamics, heat transport, and biogeochemical processes. By capturing these features, km-scale models provide more realistic representations of ocean circulation patterns and their impacts on climate (Chassignet and Xu, 2021; Fox-Kemper et al., 2019). For example, increasing horizontal resolution from 1/12° to 1/50° has been shown to significantly improve the representation of Gulf Stream separation, penetration, and variability, underscoring the substantial benefits of higher resolution in ocean modelling (Chassignet and Xu, 2017).

In addition to an eddy-rich ocean, a coupled high-resolution km-scale atmosphere (<10 km grid spacing) offers significant advantages, including improved ocean-atmosphere coupling (Sauvage et al., 2021), enhanced simulation of regional climate features through highly resolved topographic processes (Belušić and Lind, 2025; Li et al., 2024), better representation of extreme events (Kendon et al., 2021; Scoccimarro et al., 2022), and increased reliability of climate projections (Roberts et al., 2018; Schär et al., 2020). Furthermore, such km-scale coupled models bridge the gap between large-scale climate projections and local impacts, delivering globally consistent climate information at local granularity (Caldwell et al., 2021; Doblas-Reyes et al., 2025; Leutwyler et al., 2016) while advancing our understanding of ocean mesoscale eddies' role in regional climate dynamics (Chassignet and Xu, 2021; Fox-Kemper et al., 2019).

https://doi.org/10.5194/egusphere-2026-1289
Preprint. Discussion started: 21 May 2026

The benefits of high-resolution ocean models extend from short-range forecasts to climate timescales (Hewitt et al., 2017). Resolving mesoscale eddies and boundary currents reduces sea surface temperature biases and improves air-sea interactions, enhancing climate prediction skill (Beech et al., 2024; Bellucci et al., 2021). Recent studies have achieved multi-year time-slice to multi-decadal km-scale simulations (Moon et al., 2025; Rackow et al., 2025; Segura et al., 2025). However, such simulations lacked extended km-scale coupled spinup periods, crucial for assessing steady-state climate. Moreover, longer centennial timescale coupled climate simulations at such high resolution have not been performed yet, which would be useful mainly to understand the role of the ocean on the atmosphere and regional climate, as oceanic response to our climate system requires a longer timescale than just a few decades (Shi et al., 2022; Yang and Zhu, 2011). To address these limitations, we present one of the first centennial-scale km-resolution simulations using the coupled IFS-FESOM model (9 km atmosphere, 5–12 km ocean) performed under the EU project European Eddy Rich Earth System Models (EERIE). In this project, following the HighResMIP protocol (Haarsma et al., 2016; Roberts et al., 2024), we conduct a 50-year coupled spinup followed by a 100-year control as well as a 65-year historical simulation initialized from 1950 radiative conditions.

2 Model setup

The novelty of this study lies in performing a HighResMIP-style centennial-scale simulation using a climate modeling system that combines both the atmospheric model Integrated Forecasting System (IFS) and the Finite Element Sea Ice-Ocean Model (FESOM2.5) on a km scale (below 10km) resolution. A brief description of the model components is as follows:

2.1 Atmospheric Component: IFS

The atmospheric dynamics are simulated using IFS, configured on a TCo1279 octahedral reduced Gaussian grid, providing a uniform 9 km horizontal resolution globally (Rackow et al., 2025). The IFS has an integrated land and wave model and we use its version Cy48r1, implemented here using the EERIE IFS bundle DE_CY48R1.0_EERIE_20240726, which has been used for operational forecasts at the European Centre for Medium-Range Weather Forecasts (ECMWF). A schematic of the IFS model and its components in combination with the associated ocean model and I/O are shown in Figure 1.

The model employs a two-time-level semi-implicit, semi-Lagrangian time-stepping scheme, ensuring computational stability at high resolutions while maintaining accuracy in the

https://doi.org/10.5194/egusphere-2026-1289
Preprint. Discussion started: 21 May 2026

representation of atmospheric dynamics (Diamantakis and Váňa, 2022; Hortal, 2002; Temperton et al., 2001; Wedi, 2014). A hybrid, pressure-based vertical coordinate is employed, which is a monotonic function of pressure depending on surface pressure. The vertical coordinate follows terrain at the lowest level and transitions to a pure pressure-level system in the upper atmosphere. A finite-element method using cubic B-spline basis functions discretizes the vertical structure (Untch and Hortal, 2004; Vivoda et al., 2018).

The land model of IFS, ECLand (Boussetta et al., 2021), operates on the same grid as the atmosphere and is fully integrated with it through an implicit flux solver. The version of ECLand used in this work includes several components: a four-layer soil scheme, a lake model, an urban scheme, a simple vegetation model, a multi-layer snow scheme, and extensive global maps detailing various surface characteristics (Rackow et al., 2025).

Additionally, a wave model ecWAM is also integrated to account for sea-state-dependent processes within the IFS (ECMWF, 2023). This wave model operates on a reduced lat-lon grid with a resolution of 0.125°, covering 36 frequencies and directions (Rackow et al., 2025).

The IFS uses a mass-flux approach to represent deep, shallow, and mid-level convection (Tiedtke, 1989). Its microphysics scheme, based on Tiedtke, (1993), includes prognostic variables for cloud water, ice, rain, snow, and cloud fraction, with enhanced microphysical processes (Forbes and Ahlgrimm, 2014). Orographic and non-orographic gravity wave drag follow Lott and Miller, (1997), Beljaars et.al., (2004), and Orr et al., (2010). The ecRad radiation scheme (Hogan and Bozzo, 2018) performs hourly full computations on a coarse grid with frequent approximations at model resolution. These parameterizations enhance convective representation, topographic detail, and the accuracy of orographic and local circulation simulations, supporting high-resolution modelling (Rackow et al., 2025).

Our model configuration largely follows Rackow et al., (2025), with one key distinction: we retain the fully active, operational deep convection parameterization rather than reducing the cloud-base mass flux as done in that study. At 9 km horizontal resolution, deep convection remains only partially resolved, placing the model squarely in the convective “grey zone”, where the effects of relaxing the parameterization are not well established. We therefore maintain the standard formulation as the more defensible choice at this scale.

https://doi.org/10.5194/egusphere-2026-1289
Preprint. Discussion started: 21 May 2026

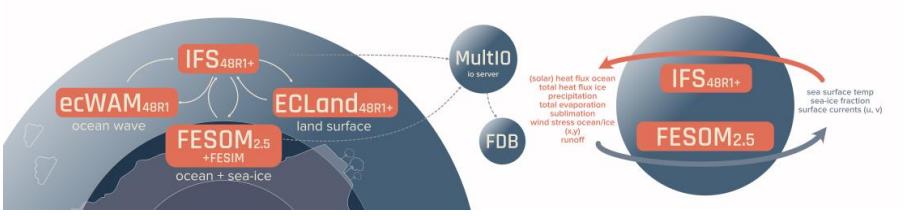

Figure 1: *Schematic of the IFS-FESOM Coupled Model System - The atmospheric model IFS (cycle 48R1) is coupled with the ocean and sea ice model FESOM2.5, the land model ECLand, and the wave model ecWAM (Rackow et al., 2025). IFS computes air-sea fluxes using surface fields provided by FESOM2.5, with coupling achieved via a sequential single-executable strategy. Output generation utilizes the MultIO framework, which optimizes parallel I/O performance for high-resolution simulations. Data storage and retrieval are managed through the Fields Database (FDB), a high-performance, scalable object-store designed for efficient access and postprocessing of model outputs.*

2.2 Oceanic Component: FESOM2.5

The Finite Volume Sea Ice-Ocean Model (FESOM) is a global ocean circulation model using unstructured meshes, allowing for flexible multi-resolution modelling (Wang et al., 2014). FESOM2.0, an updated version, employs finite volumes and arbitrary Lagrangian Eulerian vertical coordinates, improving numerical efficiency by at least 3 times while maintaining fidelity in simulations (Danilov et al., 2017; Scholz et al., 2019). The model has contributed to climate research projects and can achieve high-resolution simulations, including a 1-km Arctic Ocean configuration that adequately represents mesoscale eddies (Wang et al., 2020).

In the configuration discussed here, FESOM2.5 utilizes an unstructured mesh with variable resolution, ranging from 5 km in dynamically active meso-scale ocean eddy-rich regions over the high and mid-latitudes to coarser scales (around 11km) over the tropics. This configuration employs 70 vertical depth levels in the ocean . The name of this grid configuration is NG5 (approx. 5 million surface nodes, Rackow et al., 2025). This configuration allows for an explicit resolution of mesoscale eddies in key oceanic regions, enhanced representation of coastal processes and boundary currents, and improved simulation of sea ice dynamics, particularly in polar regions. The model's adaptive resolution helps to optimize computational resources while providing high-fidelity simulations of critical oceanic phenomena.

https://doi.org/10.5194/egusphere-2026-1289
Preprint. Discussion started: 21 May 2026

2.3 Coupling Methodology

The IFS-FESOM coupling is implemented through a single-executable framework, facilitating efficient data exchange and integration of model components (Rackow et al., 2025). The coupling strategy involves:

1. Sequential integration of atmospheric and oceanic components.
2. Hourly exchange of surface fluxes and sea surface conditions.
3. Consistent updating of boundary conditions between components.

This approach minimizes temporal inconsistencies and allows for accurate representation of rapid air-sea interactions.

2.4 Data Management and I/O Strategy

To manage the substantial data volumes generated by high-resolution simulations, the model employs an advanced I/O strategy named MultIO. It implements Fields Database (FDB) for efficient data archival and retrieval. Further details about techniques used to generate the output and other components of the IFS which facilitate this aspect can be found in Rackow et.al. 2025. We produce both high-resolution native grid outputs and perform remapping to provide a coarser, regular grid data at quarter degree resolution for various analysis requirements. Most outputs are saved in both daily and monthly frequencies. And a selected number of variables are also saved in 6 hourly frequencies based on some specific analysis requirements.

2.5 Computational performance and model throughput

The kilometre-scale IFS–FESOM configuration used in this study is computationally demanding, yet feasible for multi-decadal to centennial simulations on contemporary high-performance computing systems. The coupled model was run primarily on the JUWELS supercomputer, using approximately 300 compute nodes with 48 CPU cores per node. In this configuration, the model achieves a sustained throughput of roughly one simulated year per wall-clock day. This performance enables continuous long-term control, historical, and scenario integrations at kilometre-scale ocean resolution and ~10 km atmospheric resolution within current HPC resource allocations.

https://doi.org/10.5194/egusphere-2026-1289
Preprint. Discussion started: 21 May 2026

3 Experiments

Here we follow the HighResMIP protocol in performing the EERIE Phase 1 simulations. These simulations are part of a coordinated effort to perform kilometre-scale eddy-rich coupled climate simulations with different model configurations, enabling future multi-model comparisons.

More specifically, we conducted a 50-year coupled spin-up simulation using the Tco1279-NG5 configuration of IFS-FESOM, applying the 1950 CMIP6 radiative forcing parameters. Before commencing the coupled spin-up, we also performed a 5-year ocean-only spin-up, employing EN4 boundary forcing from the start of 1945 through the end of 1949. This preliminary step aimed to facilitate a more rapid achievement of the ocean state typical of the 1950s.

Following the completion of a 50-year coupled spin-up, we initiated two concurrent simulations: one serves as a control, while the other is a historical simulation. The historical simulation employs CMIP6 historical forcing spanning the period 1950 to 2014. Simultaneously, the control simulation was executed using constant radiative forcing from 1950. This control simulation allows us to assess any potential drift within the simulation, enabling us to exclude the influence of such drift to better understand the impact of changes in radiative forcing over time.

In the context of tropospheric aerosols, we employed the CONFESS (CONsistent representation of temporal variations of boundary Forcings in reanalyses and Seasonal forecasts) aerosol forcing (Stockdale et al., 2024), which is available from 1970 onwards and is applied in five-year epochs. For the period preceding 1970 (from 1950 to 1969), we generated epochs by replicating the 1970 aerosol forcing. This generation of aerosol forcing was conducted as part of the EU project DestinE (Destination Earth), from which additional model developments and adaptations are being integrated (Doblas-Reyes et al., 2025; Wedi et al., 2025). These efforts aim to prepare the IFS-FESOM for conducting the first operational multidecadal climate simulations on a kilometer scale.

Following the completion of the historical simulation, we extended the simulation in accordance with the SSP2-4.5 scenario pathway until 2050 to estimate near-future climate change at the kilometer scale. For this purpose, we also employed CMIP6 scenario forcings. Our estimates for tropospheric aerosols are based on the MACv2 aerosol forcing, which is subsequently adjusted to ensure compatibility with the CONFESS aerosol forcing utilized during the historical simulation.

https://doi.org/10.5194/egusphere-2026-1289
Preprint. Discussion started: 21 May 2026

The primary aim of this article is to document the performance of the historical simulation in comparison with available reanalysis and observational products. Therefore, our analysis will mainly focus on the IFS-FESOM historical simulation with some mentioning of the control simulation especially when we address the drift in the model simulation. In comparing the atmospheric fields, we will also utilize another 44-yearlong (1980-2023) AMIP simulation conducted under the EERIE project (Aengenheyster et al., Under review), using the identical atmospheric configuration of the IFS, forced with observed sea surface temperatures from the ESA-CCI SST v3 dataset at the same resolution of TCo1279 (hereafter IFS-AMIP), to specifically identify and differentiate biases associated with the atmosphere-land component of the model or those originating from the ocean component and its coupling.

4 Results

In this section, we assess the performance of the kilometre-scale IFS–FESOM simulations, progressing from global stability and feasibility, through mean climate and variability, to ocean dynamics and remaining regional biases.

4.1 A stable century-scale climate simulation at kilometre resolution

A fundamental prerequisite for global kilometre-scale climate modelling is the ability to maintain stability and avoid substantial drift over multi-decadal to centennial timescales. We therefore first assess the long-term behaviour of the coupled system using the control and historical simulations.

Figure 2 illustrates the temporal evolution of the global annual mean 2-meter temperature anomaly, which is equivalent to the global mean surface air temperature (GMSAT) across the three experiments (Control, Historical, and SSP2-4.5 scenario), as well as in the ERA5 reanalysis. A close correspondence is observed between ERA5 and the IFS-FESOM historical simulation (Fig. 2). Simultaneously, the control simulation's trajectory demonstrates only a minimal drift towards cooler temperatures as the simulation progresses, which stabilises in time. The SSP2-4.5 scenario leads to a 2 K increase in warming relative to the initial global mean temperature of the first 20 years.

https://doi.org/10.5194/egusphere-2026-1289
Preprint. Discussion started: 21 May 2026

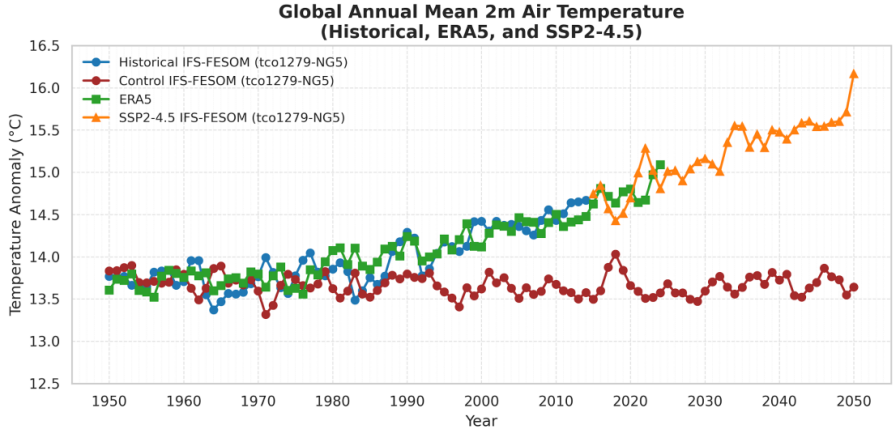

Figure 2: *Time series of annual-mean global-average 2-meter temperature (in degrees Celsius) from ERA5 reanalysis (orange), historical simulation (blue), coupled spin-up (red), and control simulation under 1950 radiative forcing (green), using the IFS-FESOM model with a 9km atmosphere and 5-11 km ocean resolution configuration.*

To place the control and historical simulations in context, we next examine the behaviour during the coupled spin-up phase. Prior to the control and historical simulations, the 50-year coupled spin-up experiment is depicted in Supplementary Figure 1. The model's GMSAT initially declines over the first 20 years of spin-up, followed by a recovery (Suppl. Fig. 1). This cooling during the spin-up is primarily attributed to the Arctic, where a rapid increase in sea ice concentration results in cooler temperatures in that region (not shown). Although this cooling trend reverses and largely stabilises by the end of the spin-up, it is not entirely eliminated and contributes to the cold bias observed in the historical simulations over the northern high latitudes (see Fig. 4).

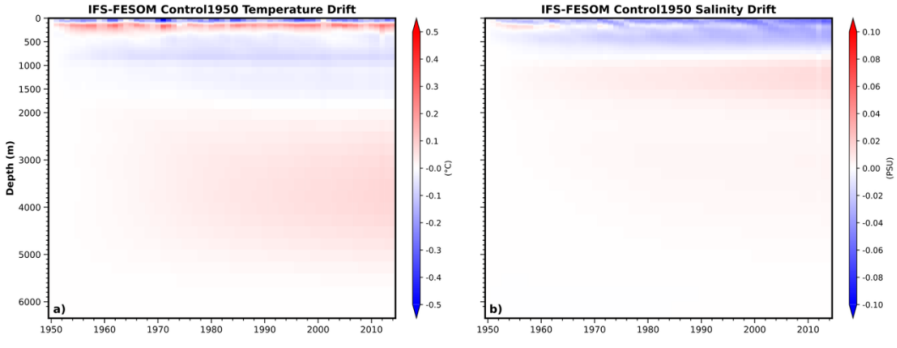

Figure 3: *Depth–time evolution of (a) ocean temperature and (b) salinity anomalies in the IFS–FESOM control simulation. Anomalies are computed as the differences between the*

https://doi.org/10.5194/egusphere-2026-1289
Preprint. Discussion started: 21 May 2026

global ocean annual-mean temperature and salinity fields at each depth and their respective values in simulation year 1.

Beyond surface temperature evolution, long-term stability of the coupled system also requires limited drift in the ocean interior. One of the primary objectives of conducting the long control simulation in parallel with the historical simulation is therefore to quantify potential drift in ocean temperature and salinity. Figure 3 illustrates the variations in the global annual mean ocean temperature and salinity at all depths throughout the simulation period. The uppermost layer of the ocean exhibits a cold bias with a maximum amplitude of approximately 0.2 to 0.3 °C; however, a persistent monotonic cooling trend is not observed (Fig. 3a). Directly beneath the uppermost layer, a warm temperature bias is evident, followed by a gradual increase in cold bias between depths of 500 and 1800 m, with a maximum amplitude of around −0.1 °C. Below 2000 m, the drift tends toward a weak warm bias with a magnitude within 0 to 0.1 °C. Regarding salinity, the upper 500–1000 m freshens by about 0.02 to 0.03 psu, while deeper layers show a gradual increase in salinity of up to 0.02 psu (Fig. 3b). It is noteworthy that the model's drift values in temperature and salinity are considerably smaller than those observed in the OMIP2 (Ocean Model Intercomparison Project phase 2) simulations (see Figure 6 of Chassignet et al., 2020), indicating that increasing resolution can substantially mitigate drift and maintain a stable oceanic state without requiring a prolonged spin-up.

To further contextualize the model's ocean temperature evolution beyond the control run, we compare the historical simulation against EN4 observations (Good et al., 2013) (Suppl. Fig. 2). Both show broadly consistent patterns of ocean heat uptake, with progressive upper-ocean warming intensifying toward the latter decades of the record, alongside a coherent intermediate-depth cooling anomaly around 700-1000 m. Differences in the early part of the record, particularly the noisier EN4 signal at intermediate depths, may partly reflect the limited subsurface observational coverage prior to the Argo era. In conjunction with the minimal drift demonstrated in the control run, this comparison reinforces confidence in the model's ability to capture large-scale ocean temperature evolution under historical forcing.

4.2 Improved large-scale surface climate relative to CMIP6-class models

To further evaluate and quantify the model's performance in comparison to previous CMIP6 simulations, we calculate the climate model performance following the approach by Reichler and Kim, (2008). More specifically, we use the methodology and parameter selection for this index proposed by Streffing et al., (2022) (Table 1). A performance value below 1 (indicated in green shades) denotes a reduction in bias relative to the CMIP6 multi-model mean, whereas

https://doi.org/10.5194/egusphere-2026-1289
Preprint. Discussion started: 21 May 2026

values exceeding 1 (indicated in red shades) suggest an increase in model bias. We utilize the historical simulation period from 1985 to 2014 to compute this table. Overall, we observe an improvement of nearly 25% over the CMIP6 multi-model means.

One of the primary issues identified is the warm bias over the southern high latitudes, characterized by elevated temperatures primarily attributed to erroneous snow depth initialization (further explanation follows). The impact of elevated temperatures over Antarctica is also evident in the summer Antarctic top-of-atmosphere outgoing longwave radiation (rlut), precipitation (pr), 500 hPa geopotential height (500 hPa zg), and 300 hPa wind (300 hPa ua). However, over the northern high latitudes, the performance index indicates an improvement in bias compared to the CMIP6 multi-model mean, as well as an enhanced representation of Arctic sea ice concentration relative to CMIP6 simulations.

Apart from the Antarctic summer period, these atmospheric parameters demonstrate improved performance globally. Notably, circulation parameters exhibit substantial improvement (darker green colors) across most regions of the world. Another critical area of focus is the Niño 3.4 region, where upper-level circulation parameters show improvements, although temperature biases persist from autumn to winter. Despite advancements in the representation of total cloud cover, biases remain in the simulation of precipitation.

In examining oceanic parameters, particularly at oceanic depths, biases are observed in the temperature at 100 meters depth and salinity at 10 meters depth in the Arctic region. This suggests potential bias in simulating Arctic sea ice at these depths, influencing the distribution of temperature and salinity. However, at greater depths and in most other regions, there is a notable improvement in the simulated ocean state compared to CMIP6 simulations.

https://doi.org/10.5194/egusphere-2026-1289
Preprint. Discussion started: 21 May 2026

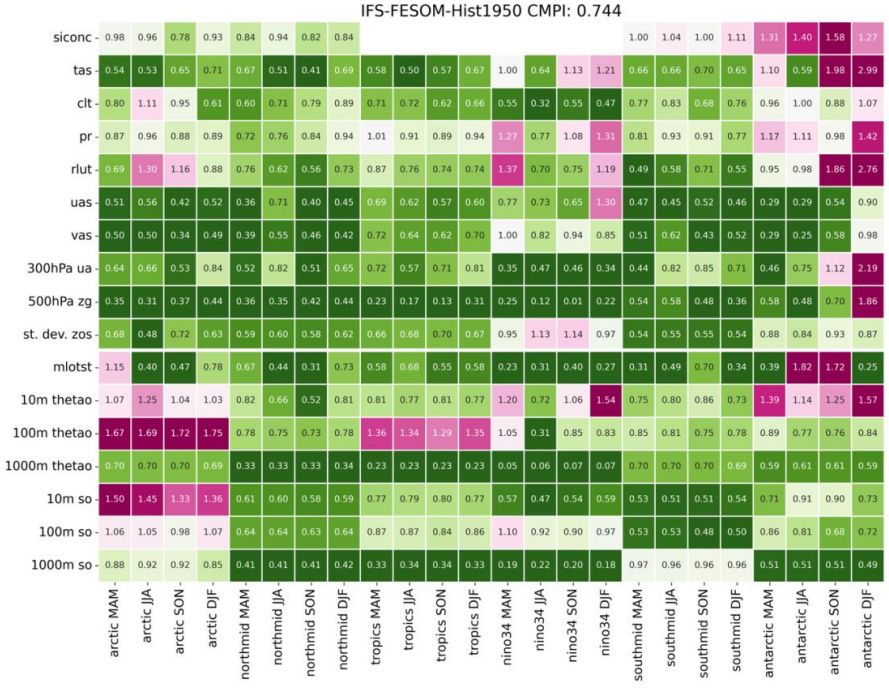

Table 1 *The performance metrics as delineated by Reichler and Kim, (2008), illustrating the absolute climatology error over the past 30 years (1985-2014) in the IFS-FESOM historical simulation. This error is expressed as a fraction of the mean absolute error across CMIP6 models. Values less than 1 denote smaller-than-average CMIP6 biases, whereas values exceeding 1 indicate larger biases. The observations employed for model evaluation include: OSI SAF OSI-450 (Lavergne et al., 2019) for sea ice concentration (siconc); MODIS Atmosphere L2 Cloud Product (Platnick , S. et al., 2015) for cloud cover (clt); Global Precipitation Climatology Project (GPCP) Monthly Analysis(Adler et al., 2018) for precipitation (pr); Clouds and the Earth's Radiant Energy System (CERES) (Wielicki et al., 1996) for TOA outgoing longwave radiation (rlut); ECMWF ERA5 reanalysis (Hersbach et al., 2020) for near-surface air temperature (tas), eastward (uas) and northward (vas) near-surface wind, 300 hPa eastward wind (ua), and 500 hPa geopotential height; NOAA Jason-1, Jason-2, and CryoSat-2 combined for sea surface height (zos); and C-GLORSv7 (Storto et al., 2016) for mixed-layer depth (mlotst) and EN4 reanalysis data for ocean temperature and salinity at various depths (Good et al., 2013). A comprehensive list of CMIP6 models considered is available in Streffing et al.(2022).*

The representation of the ocean mixed layer depth (mlotst) exhibits notable increase in performance, with the exception of the southern higher latitudes. This anomaly may be attributed to inaccuracies in the simulation of winter sea ice concentration and the formation

https://doi.org/10.5194/egusphere-2026-1289
Preprint. Discussion started: 21 May 2026

of polynyas, as previously mentioned. The standard deviation of monthly sea surface height (st. dev. zos) also exhibits significant improvements, with the exception of the Niño 3.4 region. Additionally, the tropical ocean temperature at 100 meters depth shows increased bias compared to CMIP6, which requires further investigation.

While Table 1 provides an integrated assessment of model performance across multiple variables, it does not indicate where the dominant temperature biases are geographically located. We therefore next examine the spatial structure of near-surface temperature biases to identify the regional origins of the strengths and weaknesses summarized by the performance index.

In the atmosphere, we first address the realism of the simulated 2m-temperature of the atmosphere. Figure 4a shows the climatology of the global annual mean 2m-temperature in ERA5 for the period 1985 to 2014 along with the biases for IFS-FESOM and IFS-AMIP (Fig 4b,c). In comparison to previous HighResMIP simulations (Roberts et al., 2018), temperature biases in climatology are relatively smaller from the tropics to the mid-latitudes, especially over the global ocean (Fig 4b). The pattern of biases across land regions is largely consistent between the IFS-FESOM and IFS-AMIP experiments, suggesting these biases are inherently linked to the land-atmosphere processes within the IFS model.

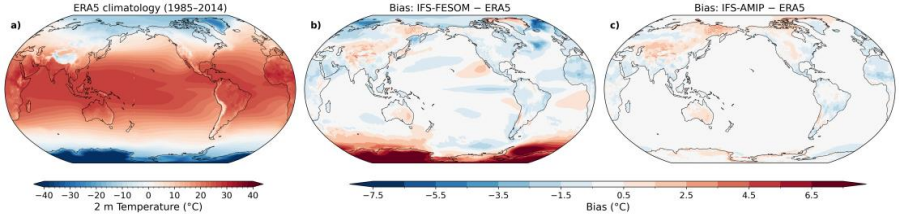

Figure 4: *Climatology of annual 2-meter temperature for the period 1985 to 2014 in a) ERA5 reanalysis and difference of the same climatology from ERA5 in b) Historical IFS-FESOM and in c) IFS-AMIP simulations. In order to account for the orographic differences between ERA5 and the model, the bias has been height-corrected using a fix adiabatic lapse rate of 6.5 °C/km (Gao et al., 2012; Remedio et al., 2019). All units are in degree Celsius.*

Many of these biases over land have been observed in previous versions of the IFS, although their magnitude appears to be reduced compared to earlier lower-resolution simulations (Roberts et al., 2018). However, the positive temperature bias observed over Central Asia, including the Himalayas and the Tibetan Plateau, appears to be new and contrary to findings

https://doi.org/10.5194/egusphere-2026-1289
Preprint. Discussion started: 21 May 2026

from previous research based on the IFS model. This bias is most pronounced during the summer compared to other seasons (Suppl. Fig. 3).

Relatively large biases in the 2-meter temperature are evident in high latitudes for IFS-FESOM, both for the control (not shown) and historical simulations. Notably, over land, there is a significant positive temperature bias observed over Antarctica and northeastern Greenland. Further analysis has confirmed that this warm bias is attributable to an error in the initial condition generation process following the coupled spin-up phase, during which the snow depth values were significantly underestimated (Suppl. Fig. 4), approximately one-tenth of their actual magnitude. This reduced snow depth resulted in anomalously warm temperatures, particularly during the summer (Suppl. Fig. 3), especially in Antarctica, where a typical 10-meter thick snow cover generally maintains much lower temperatures.

However, our analysis shows that the effect of this erroneous snow-depth initialization is confined to the Antarctic region and has less of an effect in creating temperature bias outside of the Antarctic region or other snow-covered regions (e.g. see Figure 5). Our further analysis also confirms that as the simulation progresses, the snow starts to recover by itself, although this process could take many centuries to bring snow as we expect. As the bias was discovered only after completing a substantial number of simulated years, and since its effect is restricted to a limited region, rerunning the expensive km-scale simulation was not feasible. We therefore aim to incorporate the required modifications in the next simulation cycle, benefitting also from additional insights gained during this first long km-scale coupled experiment.

Apart from Antarctica, there is also a warm bias over the Weddell Sea region, which developed during the later phase of the spinup with an accelerated increase in temperature over this region (Suppl. Fig. 5). This warm bias is seen to be strongest during the southern hemisphere winter (Suppl. Fig. 3), when we also find large negative bias in sea ice concentration and thickness (Fig. 16, 17).

We identified a cold bias over the northern high latitudes, particularly concentrated over the Nordic and Barents Seas. This bias is associated with the simulation of excess sea ice extent (see Fig. 16). Notably, the warm bias in the southern high latitudes and the cold bias, especially in the northern latitudes (as observed in Fig 4), appear to counterbalance each other, thereby maintaining the trajectory of the GMSAT in alignment with observed data throughout this period (Fig. 2).

https://doi.org/10.5194/egusphere-2026-1289
Preprint. Discussion started: 21 May 2026

In addition, a consistent cold bias was observed over the subpolar North Atlantic, potentially associated with the North Atlantic current and over the eastern to central equatorial Pacific. Some of the previously well-known temperature biases, such as the south-eastern Atlantic warm temperature bias at the coast of western Africa, were also observed; however, the magnitude was reduced from previous estimates from CMIP6 type and HighResMIP1-type model simulations (Moreno-Chamarro et al., 2022). Excluding the biases associated with higher latitudes, one of which is attributable to technical reasons (warm bias over Antarctica), the model's simulated biases demonstrated improvements in comparison to previous analogous simulations, particularly in key regions across the tropics and mid-latitudes.
To further assess whether the near-surface temperature biases identified above are associated with broader tropospheric and stratospheric structures, we next examine the zonal-mean temperature and zonal wind fields.

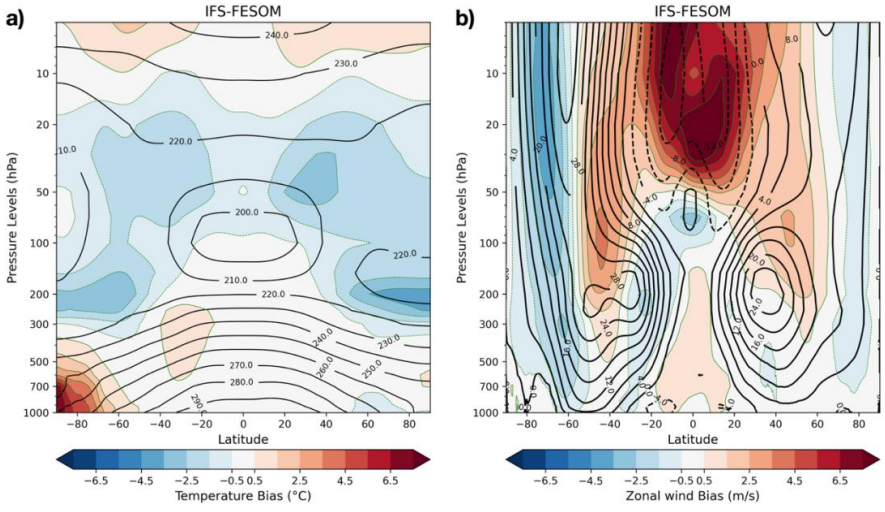

Figure 5: *Zonal mean climatology of annual mean a) temperature (in degree Celsius) and b) zonal wind (in m/s) for the period 1985 to 2014 in ERA5 (in black contours) and the bias in the same (in shading) in the IFS-FESOM historical simulation.*

Figure 5 shows the zonal-mean atmospheric temperature and zonal wind structure in the model and their biases relative to ERA5. The bias in the zonal-mean temperature structure reveals features consistent with those identified in the near-surface temperature patterns, including a warm bias over the southern high latitudes and a cold bias in the northern high latitudes. A notable improvement compared to previous IFS model generations is the reduced cold bias in the tropical lower stratosphere. Although the cold bias remains evident, it is significantly reduced and not centred over the lower stratosphere as seen in previous IFS

https://doi.org/10.5194/egusphere-2026-1289
Preprint. Discussion started: 21 May 2026

simulations (Roberts et al., 2018). Furthermore, the temperature bias in the lower to middle troposphere over the tropical to mid-latitude region is minimal. As anticipated, the bias pattern generally aligns with the findings in IFS-AMIP (Suppl. Fig. 6a), with the exception of a warm bias observed in the southern high latitudes and a less pronounced cold bias in the northern high latitudes.

In the context of mean zonal winds and associated biases, we observe a pattern consistent with previous IFS simulations (Fig. 5b). There are positive biases over the central region of the midlatitude westerly winds. However, in the subtropics and higher latitudes, the mean westerly wind appears to be weakened. The pronounced positive bias in the mid to lower stratosphere for the easterly mean zonal wind persists, as previously noted. This has been a longstanding bias typically linked to errors in the vertical diffusion of the mean zonal wind, which also affects the simulation of the Quasi-Biennial Oscillation (QBO) (Roberts et al., 2018; Streffing et al., 2022). As anticipated, a similar pattern emerges from the IFS-AMIP experiments, with the exception that the anomalous easterly wind bias over the southern high latitudes is more pronounced in the troposphere in IFS-FESOM compared to IFS-AMIP (Suppl. Fig. 6b). This may primarily result from the warm bias over Antarctica in the IFS-FESOM.

Taken together, the integrated performance metrics (Table 1), near-surface temperature patterns (Fig. 4), and zonal-mean diagnostics (Fig. 5) provide a consistent picture of improved large-scale surface climate realism relative to CMIP6-class models, with remaining biases largely confined to high-latitude regions and linked to identifiable physical and technical causes.

4.3 Persistent but reduced tropical precipitation and cloud-radiative biases

We next examine the representation of tropical precipitation and cloud-related processes, which remain among the most challenging aspects of coupled climate modelling and are closely linked to ocean-atmosphere coupling.

In the subsequent analysis, we examine the characteristics of simulated total precipitation in the model in comparison to the Multi-Source Weighted-Ensemble Precipitation (MSWEP) data (Beck et al., 2019) for the period from 1985 to 2014. Figure 6 illustrates the climatology of the annual mean total precipitation in MSWEP and the corresponding bias in our historical IFS-FESOM and IFS-AMIP simulations (Fig. 6b, c). The most prominent bias in IFS-FESOM is observed over the equatorial Pacific and the equatorial Atlantic Ocean. This bias is

https://doi.org/10.5194/egusphere-2026-1289
Preprint. Discussion started: 21 May 2026

persistent and has been identified in previous medium-resolution HighResMIP1 simulations, associated with the double ITCZ bias present in the models, which results in the bifurcation of the ITCZ center and increased precipitation on both flanks of the observed main ITCZ (Moreno-Chamarro et al., 2022). However, in the IFS-AMIP experiment the bias persists with significantly reduced magnitude compared to the coupled configuration (Fig. 6c). This suggests that equatorial Pacific sea surface temperature (SST) biases, particularly the cold tongue, play a crucial role in amplifying the double ITCZ bias.

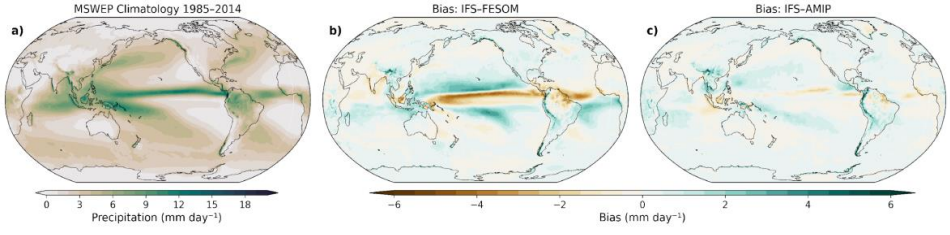

Figure 6: *Annual mean precipitation climatology for the period 1985 to 2014 in the a) MSWEP observation data (Beck et al., 2019) and the bias in the same in the b) IFS-FESOM historical simulation and c) in IFS-AMIP simulation compared to MSWEP. All units are in mm/day.*

Beyond the Pacific, a similar behaviour is found over the tropical Atlantic, where the magnitude of the precipitation bias is considerably smaller in the IFS-AMIP experiment than in IFS-FESOM. This contrast between coupled and atmosphere-only simulations is robust across seasons (Suppl. Fig. 7), highlighting the strong influence of SST biases on tropical precipitation.

Other precipitation biases, including negative precipitation over the Indian region and northeastern South America and positive precipitation biases west of South America and over the Himalayan region, are present in both IFS-FESOM and IFS-AMIP. These biases have been reported in previous HighResMIP simulations and persist here, although their magnitude appears reduced in parts of the southern and northern mid-latitudes (Table 1). Given the close coupling between precipitation, cloud cover, and surface temperature, we next assess biases in simulated total cloud cover.

https://doi.org/10.5194/egusphere-2026-1289
Preprint. Discussion started: 21 May 2026

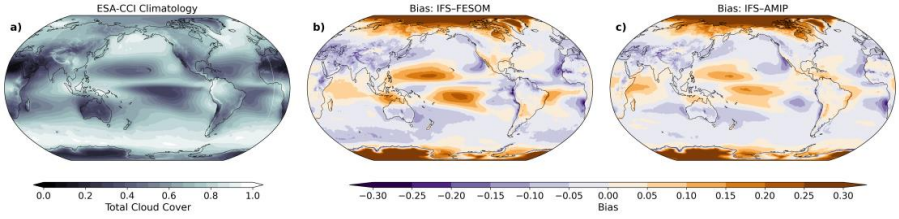

Figure 7: *Annual mean total cloud cover climatology for the period 1985 to 2014 in the a) ESA-CCI observation data (Stengel et al., 2020) and the bias in the same in the b) IFS-FESOM historical simulation and in c) IFS-AMIP simulation compared to ESA-CCI. All units are in fraction.*

Figure 7 presents the observed total cloud cover from ESA-CCI and the corresponding biases in the IFS-FESOM and IFS-AMIP experiments. The overall bias pattern closely resembles that reported in previous HighResMIP coupled simulations (Moreno-Chamarro et al., 2022), with particularly pronounced biases over the tropical Pacific and Atlantic Oceans. Regions with reduced precipitation and cooler surface temperatures generally exhibit decreased cloud cover, whereas areas with enhanced precipitation tend to show increased cloudiness. As in HighResMIP medium-resolution models, a negative total cloud cover bias persists along the west coasts of South America and Africa, although it is substantially weaker along the west coast of South America than in earlier HighResMIP simulations (Moreno-Chamarro et al., 2022; Streffing et al., 2022). This reduction is consistent with improved representation of the southeastern Pacific stratocumulus regime at higher resolution, potentially mediated by a better-resolved coastal circulation and South American orography (Richter and Mechoso, 2006).

Overall, cloud cover biases are smaller than those reported in previous HighResMIP estimates, including over midlatitude oceans, with particularly notable improvements over the North Atlantic. The relationship between negative SST biases (Fig. 12b) and reduced precipitation and cloud cover remain evident, but with reduced magnitude relative to the HighResMIP multi-model mean. This improvement is also reflected in the comparison with the CMIP6 multi-model mean (Table 1).

A further notable improvement is found over the western Indian Ocean east of Africa, where cloud cover biases are substantially reduced compared to earlier HighResMIP multi-model estimates (Moreno-Chamarro et al., 2022). Where previous models simulated cloud cover exceeding observations by up to 25% in this region, the present simulation shows biases typically limited to 10-15%, accompanied by a corresponding reduction in precipitation bias

https://doi.org/10.5194/egusphere-2026-1289
Preprint. Discussion started: 21 May 2026

(Fig. 6b). Previous low-resolution AWI-CM3 simulations (Streffing et al., 2022), which share the same ocean model component, also exhibit comparatively smaller cloud cover biases in this region, suggesting that aspects of the ocean model formulation may contribute to the reduced bias.

Outside the tropical ocean belt, cloud cover bias patterns remain largely consistent between the IFS-FESOM and IFS-AMIP experiments, indicating a weaker influence of SST biases on cloud cover. Despite these overall improvements, several key cloud cover biases persist, continuing to contribute to biases in net cloud radiative feedback.

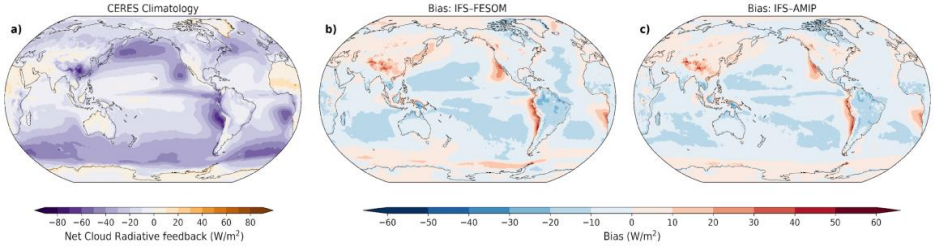

Figure 8: *Annual mean net cloud radiative feedback climatology for the period 1985 to 2014 in the a) CERES-EBAF observation data (Wielicki et al., 1996) and the bias in the same in the b) IFS-FESOM historical simulation and in the c) IFS-AMIP simulation compared to CERES-EBAF. All units are in W/m².*

Biases in cloud cover directly affect the atmospheric energy budget through their impact on radiative fluxes. We therefore next examine the net cloud radiative effect, which represents the combined shortwave and longwave influence of clouds on the Earth's energy balance. Observations indicate that clouds exert a net cooling effect globally (Fig. 8a). Both the IFS-FESOM and IFS-AMIP simulations reproduce the large-scale structure of this pattern (Fig. 8b,c), with the most pronounced differences between the two configurations occurring over the tropical Pacific and Atlantic Oceans.

Consistent with previous HighResMIP results, a positive bias in cloud radiative forcing is found in eastern boundary upwelling regions along the western coasts of South America, North America, and southern Africa. In these regions, reduced cloud cover allows increased shortwave radiation to reach the surface, contributing to local ocean warming. Notably, both the spatial pattern and magnitude of this bias are remarkably similar between the IFS-FESOM and IFS-AMIP simulations.

https://doi.org/10.5194/egusphere-2026-1289
Preprint. Discussion started: 21 May 2026

In addition, reduced cloud cover over the Himalayan and Central Asian regions results in a positive cloud radiative forcing bias, reinforcing the warm surface air temperature bias discussed in Section 4.2.

Taken together, the combined analysis of precipitation, cloud cover, and cloud radiative effects indicates that, while several long-standing tropical biases persist in the coupled simulation, their magnitude is reduced relative to previous model generations. The comparison between coupled and AMIP simulations highlights the role of ocean–atmosphere coupling in shaping tropical precipitation and cloud-related biases, while also reinforcing that cloud biases in eastern boundary upwelling regions are not primarily controlled by the underlying ocean state.

4.4 Realistic ENSO dynamics and large-scale climate variability

The El Niño–Southern Oscillation (ENSO) is the dominant mode of interannual climate variability in the tropical Pacific, characterized by sea surface temperature anomalies and associated atmospheric circulation changes (Dijkstra, 2006). Understanding ENSO mechanisms has progressed significantly through theoretical frameworks, particularly the delayed/recharge oscillator paradigm, which explains its oscillatory nature with periods of 2-7 years (Jin et al., 2020). Global climate models have played a central role in advancing ENSO understanding, with successive generations showing gradual improvements since early modelling studies of the 1980s and 1990s (Guilyardi et al., 2020). CMIP6 models outperform CMIP5 for several ENSO-relevant metrics, including improved tropical Pacific seasonality and teleconnections, although ocean surface–subsurface coupling has degraded (Planton et al., 2021).

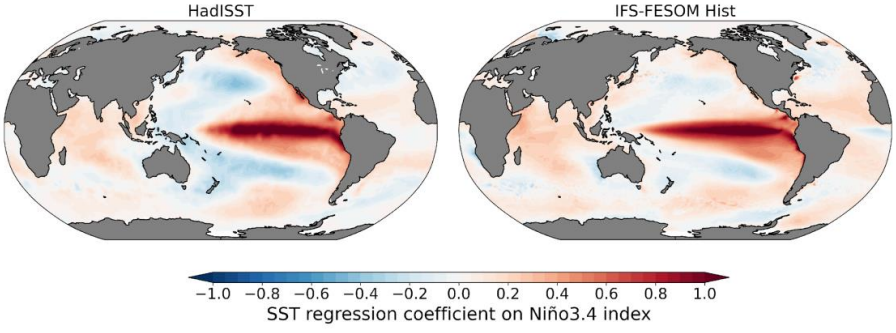

Figure 9: *The spatial regression of the sea surface temperature (SST) on the monthly Niño 3.4 index depicting the ENSO pattern in (a) HadISST, and in (b) IFS-FESOM historical simulation for the period 1950 to 2014.*

https://doi.org/10.5194/egusphere-2026-1289
Preprint. Discussion started: 21 May 2026

Figure 9 illustrates ENSO and the associated global SST pattern, as determined by the regression of SST onto the Niño3.4 index in both Hadley Centre SST observations and the IFS-FESOM simulation. Overall, ENSO-related SST anomalies and their global imprint show strong similarity between observations and the model. In particular, the ENSO footprints over the Indian Ocean and the mid- to high-latitude Pacific Ocean are well represented.

The simulated ENSO SST pattern extends further westward than observed, indicating the presence of the commonly reported westward-extended ENSO bias in climate models. In association with ENSO, the model also exhibits negative SST anomalies over the equatorial Atlantic Ocean, which are not present in observations. Over the subtropical to subpolar North Atlantic, however, the simulated ENSO-related SST pattern closely resembles observations.

The temporal characteristics of ENSO variability are further examined using the Niño3.4 index. The power spectrum of the Niño3.4 index shows a pronounced peak at periods of approximately 4-5 years in the model, in close agreement with observations (Fig. 10a). However, the amplitude of ENSO variability is more pronounced in the simulation than observed, with enhanced power persisting at lower frequencies and without the sharp decay seen in observations.

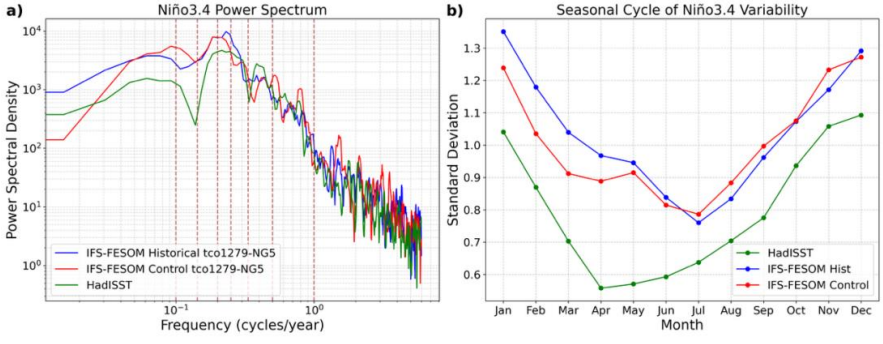

Figure 10: *a) Power spectrum of the Niño 3.4 index in the HadISST (in green) and in the IFS-FESOM Historical (in blue) and in control (in red) simulations for the period 1950 to 2014. The red dashed vertical lines indicated certain periods of cycle in years. b) for the same set of data but representing standard deviations of the monthly Niño 3.4 index. Units are in Kelvin.*

ENSO phase locking is assessed through the monthly standard deviation of the Niño3.4 index (Fig. 10b). The model successfully captures the observed phase locking, with maximum ENSO variability occurring during Northern Hemisphere winter. Nevertheless, the model places the minimum ENSO variability in mid-summer, whereas observations indicate

https://doi.org/10.5194/egusphere-2026-1289
Preprint. Discussion started: 21 May 2026

minimum variability during boreal spring. Across all seasons, ENSO variability in the model remains consistently stronger than observed.

Given that ENSO variability peaks during boreal winter, we next examine ENSO-related teleconnections in precipitation and circulation with respect to the winter Niño3.4 index. Figure 11a shows the observed association between Niño3.4 and anomalies in total precipitation and mean sea level pressure (MSLP). Positive ENSO phases are associated with enhanced precipitation over the central and eastern equatorial Pacific and reduced precipitation over the western Pacific and tropical Atlantic, together with characteristic circulation anomalies such as the Aleutian Low and a negative North Atlantic Oscillation-like pattern. The IFS–FESOM simulation captures the large-scale structure of these ENSO-related teleconnections with comparable spatial patterns and magnitudes (Fig. 11b), including the Aleutian Low over the North Pacific and a negative NAO-like response over the North Atlantic. This strong agreement is consistent with findings from a recent comprehensive multimodel assessment, which included both eddy-rich and HighResMIP simulations and identified IFS–FESOM as one of the best-performing models to date in representing late-winter extra-tropical ENSO teleconnections (Mezzina et al., 2026).

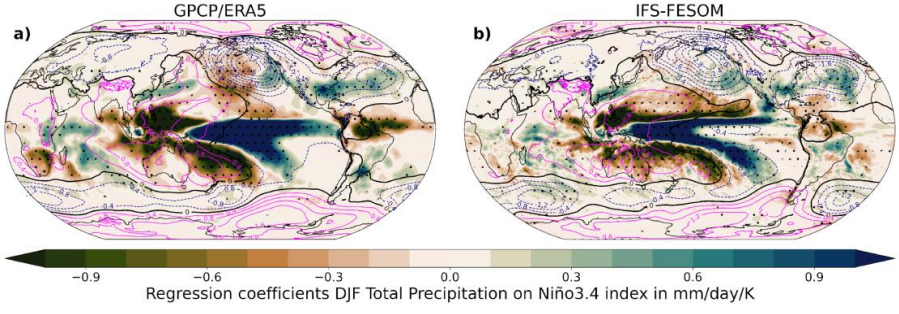

Figure 11: ***a)*** *The linear regression pattern of the winter (December-January-February, DJF) mean total precipitation (in shading) from GPCP and mean sea level pressure (on colored contours) from ERA5 on the Niño 3.4 index from HadISST for the period 1979 to 2014.* ***b)*** *is the same as in a) but from the IFS-FESOM historical simulation. The units of the shading are in mm/day/Kelvin and contours are from -4 to 4 hPa/Kelvin in 0.4hPa spacings. Negative contours are dashed colored blue and positive contours are in solid colored magenta. Stippling denotes areas where the precipitation regression coefficients are significant at the 95% confidence level.*

https://doi.org/10.5194/egusphere-2026-1289
Preprint. Discussion started: 21 May 2026

Apart from extra-tropical teleconnections, positive precipitation anomalies over the equatorial Pacific are reproduced, although anomalies over the eastern equatorial Pacific are underestimated, likely linked to biases in the simulated low-level winds. Over land, ENSO-related precipitation anomalies are generally weaker in the model than in observations. In particular, the model underestimates the dipole precipitation patterns over Africa and South America, including negative anomalies over southern Africa and positive anomalies over southeastern South America. Overall, the model effectively reproduces the main ENSO-related teleconnection patterns, particularly over the extra-tropics during winter, but it exhibits reduced amplitude in several land regions.

The North Atlantic Oscillation (NAO) is the primary mode of atmospheric circulation variability during winter and plays a critical role in shaping European climate and precipitation patterns (Hurrell et al., 2003). Consequently, accurately representing the NAO and the associated precipitation response is essential for assessing the model's ability to simulate key modes of large-scale atmospheric variability.

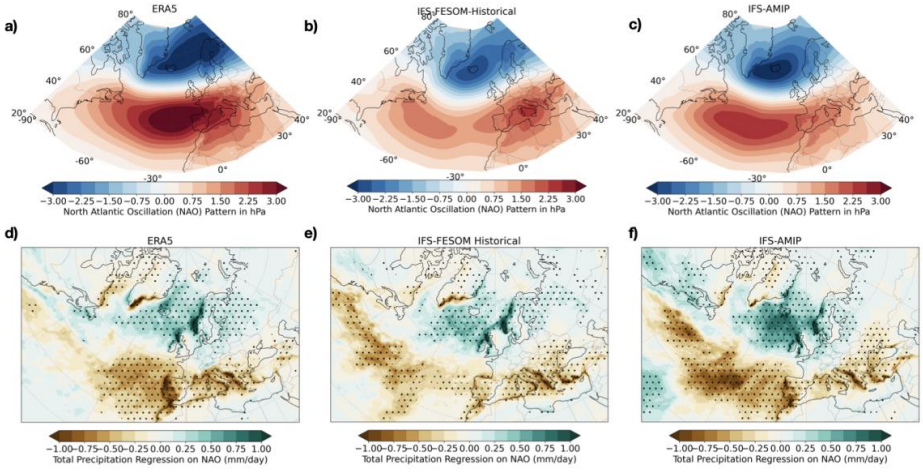

Figure 12: *The spatial pattern of the leading mode of winter mean sea level pressure variability over the domain (20-80N and 90W to 40E) known as the North Atlantic Oscillation in a) ERA5, in b) the IFS-FESOM historical simulation and in c) IFS-AMIP experiment. d), e) and f) are the linear regression pattern of the total precipitation (in mm/day) on to the normalised principal component time series associated with the winter NAO pattern. Over the stippled regions the patterns are significant at 95% level.*

Figure 12a illustrates the winter NAO pattern in ERA5, which represents the leading mode of mean sea level pressure (MSLP) variability over the North Atlantic–European sector. The

https://doi.org/10.5194/egusphere-2026-1289
Preprint. Discussion started: 21 May 2026

positive phase of the NAO is characterized by a low-pressure anomaly centered near Iceland and a high-pressure anomaly centered over the Azores. The associated total precipitation response, derived by regressing precipitation onto the normalized principal component time series of this leading mode, is shown in Figure 12d. It reveals positive precipitation anomalies over Northern and Western Europe and negative precipitation anomalies over Southern and Southwestern Europe, extending over adjacent oceanic regions.

In the IFS-FESOM simulation, the model successfully captures the strength and location of the low-pressure anomaly center of the winter NAO (Fig. 12b). However, it underestimates the strength of the high-pressure anomaly, and the center of this anomaly appears split, with one center over the Mediterranean Sea and another over the mid-North Atlantic. This deviation from the observed NAO structure results in the model's inability to capture the negative precipitation anomalies over Southwestern Europe, particularly along the coastlines of Portugal and Spain (Fig. 12e). In contrast, the model performs well in capturing the positive precipitation anomalies over Northwestern Europe.

We further examine the NAO in the IFS-AMIP experiments to assess the extent to which these biases are linked to the atmospheric model itself or to coupled ocean–atmosphere interactions. Under observed SST conditions and without two-way coupling, the IFS model simulates the location of the positive MSLP anomaly of the winter NAO more realistically (Fig. 12c). Consequently, the associated negative precipitation anomalies over Southwestern Europe are better represented compared to IFS-FESOM (Fig. 12f). Although the amplitude of both positive and negative MSLP anomaly centers remains slightly underestimated, the overall NAO structure in IFS-AMIP shows closer agreement with ERA5.

The findings indicate that biases in SST patterns over the subpolar North Atlantic, along with their interaction with the atmosphere, may contribute to the formation of the southern positive anomaly branch of the winter NAO and its related precipitation response. Additionally, external influences, such as the ENSO teleconnection, may also play a role, as its regional impact over the North Atlantic aligns with the mid-North Atlantic center of the southern NAO signal during this period.

4.5 Realistic emergence of mesoscale eddies and western boundary currents

One of the key advantages of kilometre-scale ocean resolution is the explicit representation of mesoscale eddies and their interaction with large-scale circulation features, particularly

https://doi.org/10.5194/egusphere-2026-1289
Preprint. Discussion started: 21 May 2026

western boundary currents. Here, we assess the extent to which the IFS-FESOM configuration resolves mesoscale eddy activity and captures its spatial structure and scaling characteristics. We first examine the standard deviation of daily sea surface height (SSH) as a measure of mesoscale eddy activity, comparing the IFS-FESOM simulation with satellite-based observations from the AVISO dataset (Fig. 13). In the observations, elevated SSH variability highlights the primary eddy-rich regions of the global ocean, including the Gulf Stream and Kuroshio current systems, the Agulhas and Benguela regions, and the Southern Ocean.

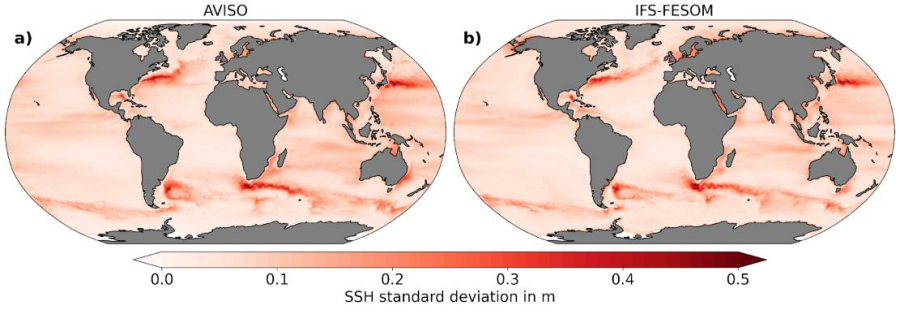

Figure 13: *The daily SSH standard deviation over the period 1993 to 2014 in a) AVISO and in b) IFS-FESOM Historical simulation highlighting the ocean eddy-rich regions. Units are in meters.*

The IFS-FESOM simulation reproduces both the magnitude and the spatial distribution of SSH variability remarkably well across these regions, indicating that mesoscale eddy activity is realistically represented at the chosen resolution. One notable exception is found in the Gulf Stream region, where the simulated SSH variance exhibits a more zonal orientation than observed, reflecting a more zonally oriented North Atlantic Current in the model.
This bias in current orientation is consistent with the cold sea surface temperature bias observed in the subpolar North Atlantic (Fig. 15b) and is a common feature of many coupled climate models. Nevertheless, the overall agreement in SSH variance demonstrates that the model captures the global pattern of eddy activity with high fidelity.

https://doi.org/10.5194/egusphere-2026-1289
Preprint. Discussion started: 21 May 2026

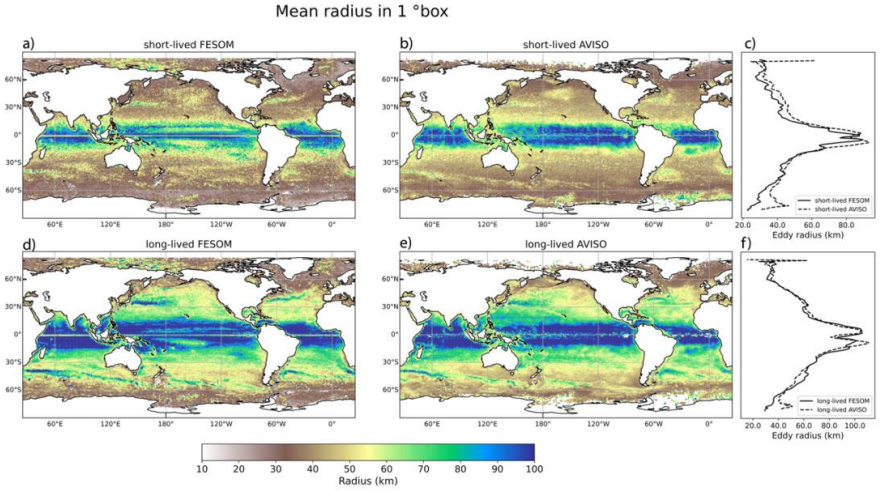

Figure 14: *Mesoscale eddy mean radius in 1-degree boxes for short-lived eddies (lifetime 10-30 days) in FESOM (a) and observations (b) and long-lived (lifetime >30 days) eddies in FESOM (d) and observations (e). Zonal mean radius for short-lived (c) and long-lived (f) eddies of the model (solid) and observations (dashed).*

To further evaluate the realism of simulated eddies, we analyse the characteristic radii of both long-lived and short-lived eddies and compare them with observational estimates derived from the META3.2 two-satellite eddy dataset produced by AVISO (Fig. 14). In both observations and the model, long-lived eddies exhibit larger radii than short-lived eddies, consistent with theoretical expectations that more energetic eddies can grow to larger spatial scales.

The simulated eddy radii follow the expected latitudinal scaling with the first baroclinic Rossby radius of deformation, indicating that the model captures the fundamental dynamical controls on eddy size. Deviations from this scaling occur near the equator, where geostrophic balance breaks down and linear theory is no longer applicable; this behaviour is reproduced by the model. Zonal-mean comparisons show good agreement between simulated and observed eddy radii across most latitudes, with larger discrepancies in polar regions. In the Southern Ocean, observed zonal-mean eddy radii appear larger than those in the model, likely reflecting limitations of satellite observations at high latitudes, where the Rossby radius becomes small and eddy detection is more uncertain.

An additional advantage of the model is its ability to identify and track eddies beneath sea ice, which is not possible using satellite observations. This capability explains the absence of

https://doi.org/10.5194/egusphere-2026-1289
Preprint. Discussion started: 21 May 2026

observational eddy-radius estimates in polar regions and highlights the added value of high-resolution coupled simulations for diagnosing polar ocean dynamics.

A notable discrepancy between the model and observations is the presence of two zonal bands of reduced eddy radii on either side of the equator in the observational dataset, which are less pronounced in the model. The origin of this feature remains unclear and may be related to equatorial current dynamics or to the splitting of the Intertropical Convergence Zone; further investigation is required to clarify its cause.

Overall, the realistic representation of SSH variability, the correct latitudinal scaling of eddy radii, and the coherent depiction of eddy-rich regions demonstrate that the IFS-FESOM configuration operates in an eddy-rich regime. This explicit representation of mesoscale dynamics provides a physically consistent foundation for improved simulation of western boundary currents and their role in large-scale ocean-climate interactions.

4.6 Improved ocean state with persistent polar mixed-layer depth biases

We next examine the simulated mean ocean state, focusing on sea surface temperature, sea surface salinity, and mixed-layer depth, which together govern air–sea heat and freshwater exchanges and strongly influence large-scale ocean circulation and climate variability. SST is a key variable for the climate system, as it regulates air–sea heat exchange, sea ice formation, and storm development. Figure 15a shows the observed mean SST climatology from the ESA SST CCI dataset for the historical period 1985–2014 (Merchant et al., 2019), characterized by strong meridional gradients, sharp fronts along western boundary currents, and cold SST anomalies in major upwelling regions.

https://doi.org/10.5194/egusphere-2026-1289
Preprint. Discussion started: 21 May 2026

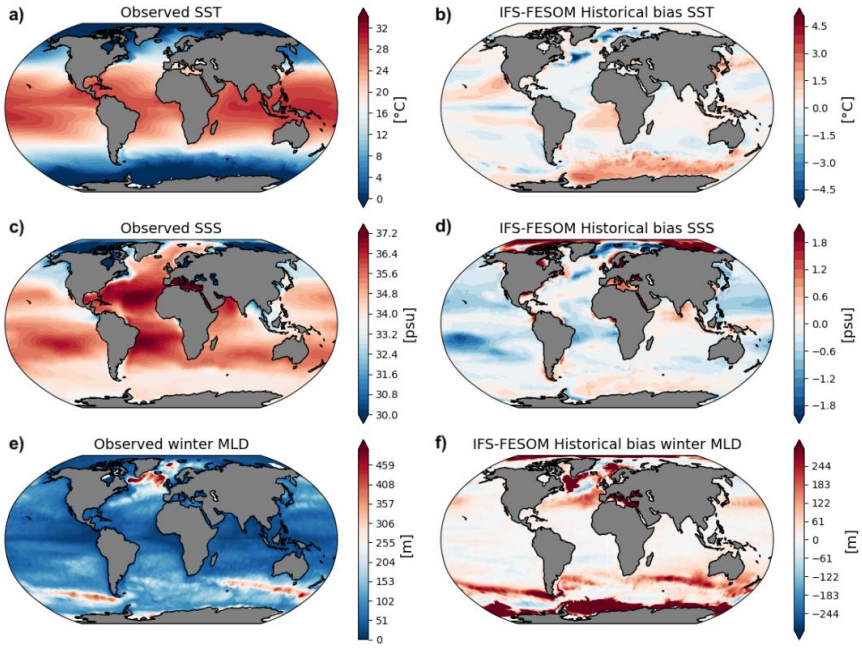

Figure 15: *(a) Mean (1985-2014) Sea Surface Temperature (SST) from ESA SST CCI (Merchant et al., 2019); (b) SST mean bias in IFS-FESOM relative to the observations over the period 1985-2014. (c) Mean (1985-2014) Sea Surface Salinity (SSS) from EN4 (Good et al., 2013). (d) SSS mean bias in IFS-FESOM relative to the observations over the period 1985-2014. (e) Mean (1985-2014) winter Mixed-Layer Depth (MLD) from de Boyer Montégut (2022) climatology. (f) MLD winter bias in IFS-FESOM relative to the observations over the period 1985-2014. All biases are computed as model minus observations.*

Relative to observations, the IFS-FESOM simulation exhibits a warm SST bias of up to approximately 2.5 °C in the Southern Ocean (Fig. 15b), a feature also present in the CMIP6 multi-model mean (Fox-Kemper et al., 2021). Warm biases of around 1-1.5 °C are found in eastern boundary upwelling systems such as the Benguela and California regions, with a weaker bias in the Peru-Chile upwelling system. A pronounced cold SST bias of up to -4.5 °C is evident in the northwestern Atlantic. Overall, the magnitude of SST biases in IFS-FESOM however appears reduced compared to the CMIP6 multi-model mean, particularly in midlatitude regions, consistent with improvements in the representation of mesoscale dynamics and boundary currents discussed in Section 4.5.

Sea surface salinity (SSS) reflects changes in the global water cycle and provides an integrated measure of evaporation-precipitation balance and freshwater input. It also influences stratification in subpolar and polar regions (Caneill et al., 2022). Salinity anomalies

https://doi.org/10.5194/egusphere-2026-1289
Preprint. Discussion started: 21 May 2026

are transported by ocean eddies (e.g., Agulhas, North Brazil Current, Gulf Stream rings), leading to differing SSS biases between eddy-rich and non-eddying models. We compare simulated SSS with the EN4 observational dataset (Good et al., 2013). The observed SSS climatology is characterized by high salinities in subtropical gyres and semi-enclosed basins, and low salinities in the Arctic, near major river outflows, and along the Intertropical Convergence Zone (Fig. 15c).

The IFS-FESOM simulation shows pronounced positive SSS biases in the Arctic Ocean (Fig. 15d), although salinity in this region is subject to considerable observational uncertainty (Liu et al., 2022). Positive SSS biases are also found in semi-enclosed seas such as the Mediterranean, Baltic, and Red Seas, as well as near the mouths of major rivers. In contrast, the model exhibits a predominantly negative SSS bias across the tropical and subtropical open ocean, like the CMIP6 models. A notable improvement relative to CMIP6 simulations is the absence or strong reduction of the widespread fresh bias in the Southern Ocean (Eyring et al., 2021; Liu et al., 2022), which may be linked to improved representation of advective processes in the Antarctic Circumpolar Current or to changes in simulated evaporation and precipitation.

The ocean mixed layer forms the interface between the atmosphere and the ocean interior and plays a central role in regulating heat, freshwater, and momentum exchange. We evaluate the simulated mixed-layer depth (MLD) against a climatology derived from in situ observations (de Boyer Montégut, 2023; de Boyer Montégut et al., 2004), mainly from ARGO and World Ocean Databas. Following (Fox-Kemper et al., 2021), we define MLD as the depth where potential density is 0.03 kg m-3 denser than at 10m, with winter MLD as the mean of January-March for Northern Hemisphere and July-September for Southern Hemisphere.

IFS-FESOM shows deep winter MLD biases of hundreds of meters in the Labrador and Greenland Seas, Mediterranean and Black Seas, and in parts of Antarctic Circumpolar Current (Fig. 15f). The most prominent MLD bias occurs in the Weddell Sea, where the model simulates unrealistically deep winter mixed layers. This bias is absent in the CMIP6 multi-model mean and may be linked to biases in winter sea ice concentration (see Fig. 16, 17) and the potential formation of polynyas. It should be noted, however, that observational constraints on Southern Ocean MLD remain limited due to sparse in situ data (de Boyer Montégut, 2023).

Taken together, the simulated mean ocean state in IFS-FESOM shows overall improvements in SST and SSS relative to CMIP6-class models, while mixed-layer depth biases persist in

https://doi.org/10.5194/egusphere-2026-1289
Preprint. Discussion started: 21 May 2026

specific regions, most notably in the Southern Ocean. These results highlight both the benefits of increased resolution for representing ocean structure and the remaining challenges associated with air-sea ice interactions.

4.7 Contrasting polar sea-ice characteristics and high-latitude climate biases

We next examine the simulated sea-ice state and associated high-latitude surface climate, focusing on the Arctic and Antarctic regions. Sea ice plays a central role in the climate system through its influence on surface albedo, ocean-atmosphere heat exchange, and freshwater fluxes, and remains a key source of uncertainty in coupled climate models.

Figure 16 shows the climatology and biases of sea ice concentration (SIC) in the IFS-FESOM historical simulation relative to observations. In the Arctic, the model exhibits a persistent positive SIC bias, particularly in the Nordic and Barents Seas (Fig. 16a). This bias is closely linked to an overestimation of sea ice extent, with the model simulating ice cover that extends further south than observed. The excess Arctic sea ice results in reduced ocean-atmosphere heat exchange and contributes to a pronounced cold surface temperature bias over the northern high latitudes, consistent with the near-surface temperature biases discussed in Section 4.2. Despite this cold bias, the Arctic SIC performance represents an improvement relative to the CMIP6 multi-model mean, as reflected in the performance metrics summarized in Table 1.

In contrast to the Arctic, the Antarctic sea ice biases show a more complex spatial structure. During the Southern Hemisphere winter (September), the model simulates negative SIC biases over the eastern Weddell Sea and adjacent regions, while positive SIC biases are found to the west of the Weddell Sea (Fig. 16b). Although the positive SIC bias can largely be attributed to the model's simulation of a larger SIC extent compared to observations, the negative SIC bias coincides with a pronounced warm sea surface temperature bias in the same region (Fig. 15b), suggesting enhanced oceanic heat fluxes and the formation of polynyas that inhibit sea ice growth.

https://doi.org/10.5194/egusphere-2026-1289
Preprint. Discussion started: 21 May 2026

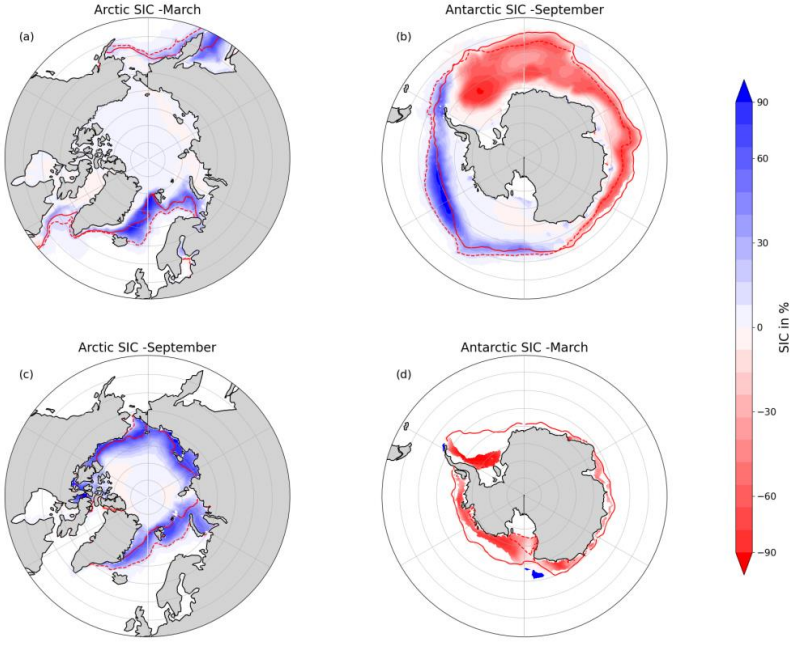

Figure 16: *The difference between IFS-FESOM model and observed (OSI-SAF) sea ice concentration (SIC) based on climatology (Lavergne et al., 2019) from 1985-2014 period for Arctic winter (a) Antarctic winter (b) Arctic summer (c) and Antarctic summer (d). The red solid and dashed linse show the climatological sea ice extent (where SIC is 15%) from observations (OSI-SAF) and the IFS-FESOM respectively.*

During the Antarctic summer (March), the model generally underestimates sea ice concentration and extent across much of the Southern Ocean (Fig. 16d). This discrepancy may be attributed to the relatively higher temperatures over the Antarctic during summer as represented in the model (Suppl. Fig. 3). This may also be attributed to the air-sea ice fractional coupling scheme implemented in this simulation, which could potentially inhibit sea ice formation or retention during the summer months (further explanation follows).

Beyond sea-ice concentration, the coupled IFS-FESOM simulation exhibits pronounced regional biases in sea-ice thickness (Fig. 17). In the Arctic, ice thickness is systematically overestimated, with the largest positive biases occurring in the central to western Arctic and exceptionally strong maxima over the channels and gaps of the Canadian Arctic Archipelago, particularly in the Queen Elizabeth Islands region (Fig. 17a,c). The Arctic thickness bias increases with integration time (not shown), indicating a progressive departure from the observed mean state. In contrast, Antarctic sea ice is systematically thinner than observed

https://doi.org/10.5194/egusphere-2026-1289
Preprint. Discussion started: 21 May 2026

(Fig. 17b,d), most clearly during the winter growth season, while the spatial pattern of ice concentration remains comparatively realistic (Fig. 16b). These opposing hemispheric thickness biases persist throughout the coupled integration and are robust across averaging periods.

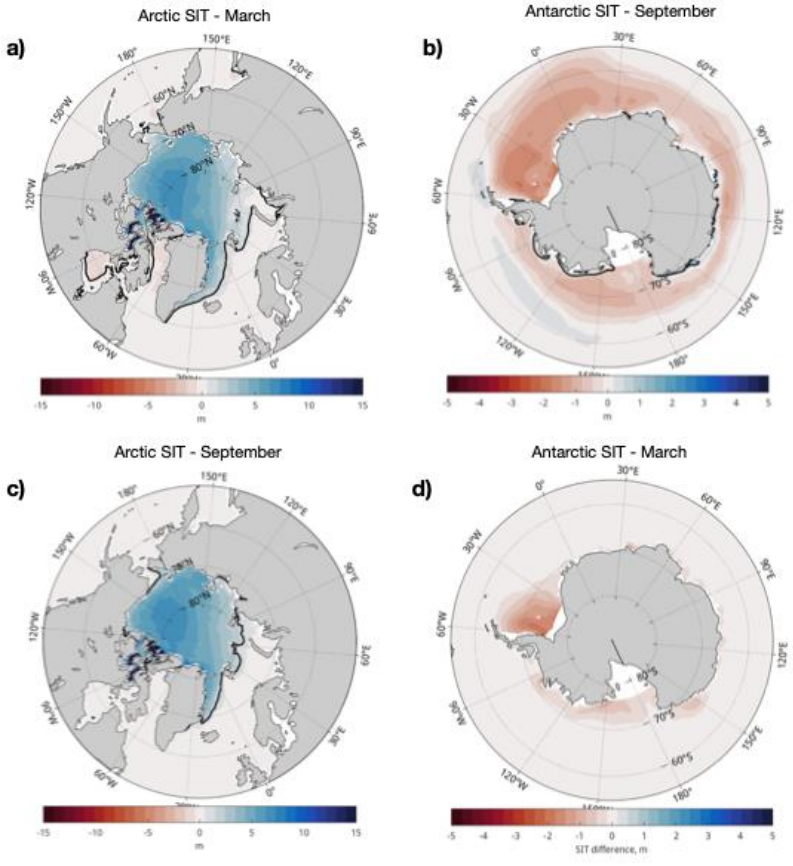

Figure 17: *The difference between the IFS-FESOM model and observed (GEOMAS) sea ice thickness (Zhang and Rothrock, 2003) based on climatology from 1999-2014 period for Arctic winter (a) Antarctic winter (b) Arctic summer (c) and Antarctic summer (d). The dark blue solid line shows the climatological sea ice thickness of 1.5meters in IFS-FESOM.*

The interpretation of the bias stems from the coupling formulation and thermodynamic principles of sea ice. Sea ice is coupled fractionally between atmosphere and ocean through sea-ice concentration, while the atmospheric surface scheme uses a fixed 1.5 m ice thickness for ice-covered regions. Hence the surface fluxes are computed using uniform thermal resistance, independent of simulated ice-thickness distribution, affecting vertical heat conduction representation.

https://doi.org/10.5194/egusphere-2026-1289
Preprint. Discussion started: 21 May 2026

Conductive heat flux through sea ice varies inversely with thickness: thin ice allows strong upward heat flux, while thick ice insulates the ocean (Liu and Zhang, 2025; Maykut, 1986). Therefore, a fixed 1.5 m thickness can misrepresent winter heat loss when ice is much thicker or thinner. Over thick ice, excessive heat loss occurs as the atmosphere treats it as too thin, while over thin ice, winter heat loss is suppressed as it's treated as overly insulating. This thickness-dependent response explains the contrasting hemispheric behaviour. In the Arctic, where multi-year thick ice dominates, enhanced winter heat loss leads to progressive ice thickening over time. In the Antarctic, where sea ice is predominantly seasonal with less than 1.5 thickness and more sensitive to oceanic heat fluxes, suppressed winter growth yields systematically thinner ice.

Although surface and conductive heat fluxes are not explicitly diagnosed here, the sign and hemispheric contrast of the simulated thickness biases are consistent with the expected thermodynamic response to the fixed-thickness assumption. A targeted flux diagnosis would be a useful next step to quantify this contribution.

4.8 Realistic AMOC strength and large-scale overturning circulation

We finally assess the representation of the Atlantic Meridional Overturning Circulation (AMOC), a key component of the global ocean circulation that transports heat from low to high latitudes and strongly influences the climate of the North Atlantic region and Europe. Figure 18a shows the climatology of the AMOC stream function in depth coordinates from the IFS–FESOM historical simulation. The model simulates a maximum AMOC strength of approximately 20 Sv at depths of 1000-1200 m and around 35°N, associated with the upper overturning cell.

Compared to earlier FESOM configurations at lower resolution, the simulated AMOC strength is enhanced by approximately 1-2 Sv, indicating a strengthening of the overturning circulation with increasing horizontal resolution. This behaviour is consistent with improved representation of boundary currents and mesoscale processes discussed in Section 4.5.
To further evaluate the realism of the simulated AMOC, we compare the modelled overturning strength at 26.5°N with observations from the RAPID array (Fig. 18b). The simulated AMOC strength at this latitude lies within the observed range, with values of approximately 17-20 Sv, and captures the correct order of magnitude of the observed circulation.

https://doi.org/10.5194/egusphere-2026-1289
Preprint. Discussion started: 21 May 2026

The time evolution of the AMOC at 26.5°N shows a gradual weakening over the historical period, which is consistent with the expected response of the overturning circulation to anthropogenic forcing. While the observational record remains relatively short, the simulated decline is comparable in magnitude to trends inferred from the RAPID observations. Overall, the realistic magnitude of the AMOC and its sensitivity to increased resolution indicate that the IFS–FESOM configuration provides a credible representation of large-scale overturning dynamics, supporting its suitability for investigating the role of mesoscale processes in ocean–climate interactions.

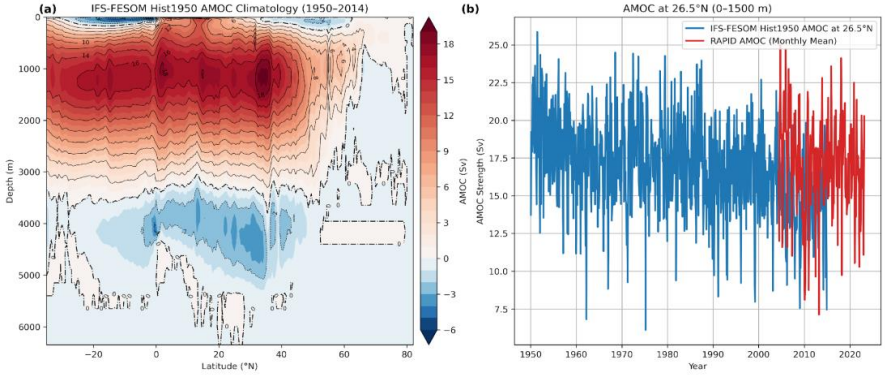

Figure 18: *a) Atlantic Meridional Overturning circulation stream function (in Sv) on depth space from the IFS-FESOM EERIE historical simulation and b) is the time series of the monthly mean AMOC stream function between 0 to 1500m time at 26.5N (in blue) and the same from the observed RAPID observations array (in red).*

5 Discussion:

The kilometre-scale IFS–FESOM simulation demonstrates a substantial improvement in climate performance relative to typical CMIP6-class models. Across a broad range of atmospheric and oceanic fields, biases are generally reduced compared to the CMIP6 multi-model mean (Table 1). Long-standing errors, such as warm SST biases in eastern boundary upwelling regions and the cold bias in the subpolar North Atlantic, are present but noticeably diminished. Large-scale circulation metrics, including near-surface winds and sea-level pressure, show particularly noticeable improvements, while cloud cover biases are reduced globally. Tropical precipitation biases, including the double ITCZ, persist but with reduced magnitude. In the ocean, temperature and salinity fields outside the polar regions compare more closely with observations than in standard-resolution models. These results indicate that resolving mesoscale ocean dynamics and employing a ~10 km atmospheric grid can improve the simulated mean climate state in long coupled integrations.

https://doi.org/10.5194/egusphere-2026-1289
Preprint. Discussion started: 21 May 2026

A key outcome of this experiment is the ability of the coupled km-scale model to maintain climate stability over the full simulation period. Following a 50-year high-resolution spin-up, the coupled system exhibits only weak drift in global ocean temperature and salinity, with magnitudes considerably smaller than those reported in lower-resolution experiments (Fig. 13). This suggests that increased resolution can alleviate some of the long-standing equilibration challenges in coupled climate models, likely through improved representation of ocean circulation and mixing. The demonstrated stability of this centennial-scale simulation represents an important step forward and highlights the feasibility of long-term global integrations at kilometre-scale resolution.

Despite these overall improvements, persistent high-latitude biases highlight key challenges. In Antarctica, a pronounced warm near-surface temperature bias was traced to an error in snow initialization. In the Southern Ocean, particularly the Weddell Sea region, warm biases, reduced sea-ice concentration, and excessively deep winter mixed layers indicate overly strong convection and polynya-like behaviour. Notably, such an extreme Weddell Sea mixed-layer bias is not present in the CMIP6 multi-model mean, suggesting that the higher resolution or coupling strategy employed here may expose new sensitivities in Southern Ocean processes that require targeted investigation. Sparse observations complicate validation, but the magnitude of the bias warrants closer examination of ocean mixing and ice-ocean interactions.

In contrast, the Arctic exhibits a cold bias linked to excessive sea-ice extent, particularly in the Nordic and Barents Seas. While similar biases are common in CMIP6 models, their magnitude is reduced in the present simulation (see Table 1). The Antarctic warm bias and Arctic cold bias partially offset each other in the global mean surface temperature, resulting in a realistic global temperature evolution. However, this compensation is fortuitous and emphasizes the need for improved sea-ice thermodynamics and coupling strategies to reduce regional errors in both hemispheres.

Persistent warm biases in near-surface air temperature and sea surface temperature over continental shelves during summer have also been quantified for this simulation, reaching up to 6 °C in SST and 4 °C in air temperature (Delpech et al., 2025). These biases have been attributed to the absence of tidal mixing associated with the dissipation of barotropic tides on continental shelves at the global scale, highlighting the need for further model developments to represent these processes.

Beyond the mean state, the km-scale configuration shows notable skill in representing internal climate variability. ENSO is simulated with realistic spatial structure, temporal variability, and seasonal phase locking, although the model exhibits slightly enhanced variance compared to

https://doi.org/10.5194/egusphere-2026-1289
Preprint. Discussion started: 21 May 2026

observations. ENSO-related teleconnections, including precipitation and sea-level pressure responses over the Pacific and North Atlantic, are realistically represented, though some land-based teleconnections remain weaker than observed. These results suggest that resolving finer-scale air–sea interactions contributes to a more faithful representation of coupled modes of variability.

The eddy-rich ocean component produces a dynamically active circulation that closely resembles observations. Mesoscale eddy activity is realistically simulated across major current systems, and eddy size distributions broadly follow theoretical expectations based on the Rossby radius. One remaining limitation is a slightly too-zonal Gulf Stream pathway, which contributes to residual cold biases in the subpolar North Atlantic. Large-scale ocean circulation is also well captured: the Atlantic Meridional Overturning Circulation exhibits a realistic strength and vertical structure, with values at 26.5°N comparable to RAPID observations and a gradual weakening under historical forcing.

The ocean mixed-layer depth remains a key area for improvement. While stratification is generally reasonable across most basins, excessively deep winter mixed layers in known deep-convection regions, particularly the Weddell Sea, point to sensitivities in convective and ice–ocean processes at high resolution. Importantly, despite these intense regional convection events, the coupled system remains stable and does not exhibit runaway drift, reinforcing the robustness of the km-scale configuration.

Key limitations of this study should be acknowledged. The use of a single high-resolution configuration prevents a clean attribution of improvements to resolution alone, as opposed to model formulation or tuning. Planned multi-resolution experiments with IFS–FESOM will help disentangle these effects. At the same time, specific issues identified here, including the Antarctic snow initialization error and sea-ice biases, provide clear targets for future development. The reduction of several long-standing regional biases nevertheless suggests that resolving mesoscale processes yields tangible benefits for climate fidelity.

Conclusions

This study demonstrates that global coupled climate simulations at kilometre-scale resolution are feasible over multi-decadal to centennial timescales and can be conducted without strong climate drift. The IFS–FESOM configuration achieves a more realistic representation of the mean climate state and key modes of variability than typical CMIP6-class models, with notable improvements in large-scale circulation, mesoscale ocean dynamics, ENSO behaviour, and Atlantic overturning strength.

https://doi.org/10.5194/egusphere-2026-1289
Preprint. Discussion started: 21 May 2026

At the same time, higher resolution does not eliminate all biases. Instead, it exposes new sensitivities, particularly in polar regions, where sea-ice processes, ocean mixing, and coupling strategies play a dominant role, and in coastal regions, where unresolved processes such as tidal mixing can influence the local climate state. These results highlight that advancing toward km-scale Earth system models must be accompanied by continued development of physical parameterizations and coupling approaches, especially for ice-ocean-atmosphere interactions.

Overall, our findings indicate that eddy-rich, kilometre-scale coupled models provide a physically richer and more faithful framework for simulating the climate system. As computational resources expand, such configurations offer a promising pathway toward next-generation climate models capable of delivering improved regional and global climate projections.

Code Availability

The ocean and sea-ice model FESOM2.5 is available at https://doi.org/10.5281/zenodo.10225420 (Rackow et al., 2023) and from GitHub at https://github.com/FESOM/fesom2. The atmospheric model IFS is proprietary software available subject to a licence agreement with ECMWF, with access granted to member-state weather services and approved research partners. The IFS code without data assimilation modules is also available under an openIFS licence for educational and academic purposes (http://www.ecmwf.int/en/research/projects/openifs). The IFS cycle used in this study was CY48R1.

Data Availability

The model simulation data used in this study are openly available from the World Data Center for Climate (WDCC). The coupled spin-up simulation is available at https://www.wdc-climate.de/ui/entry?acronym=DKRZ_LTA_1344_dsg0001 (Ghosh et al., 2024). The historical simulation data are available at https://doi.org/10.26050/WDCC/EERIE_FESOM_hist_v1 (Ghosh et al., 2025a), and the SSP2-4.5 scenario simulation data are available at https://doi.org/10.26050/WDCC/EERIE_FESOM_s245_v1 (Ghosh et al., 2025b).

ERA5 reanalysis data were obtained from the Copernicus Climate Data Store (https://cds.climate.copernicus.eu). Observed sea surface height data from AVISO were obtained from the Copernicus Marine Data Store (https://marine.copernicus.eu). Observational mixed-layer depth climatologies were obtained from the dataset of de Boyer Montégut (2023), available at https://doi.org/10.17882/91774.

Precipitation observations were taken from the Multi-Source Weighted-Ensemble Precipitation (MSWEP) dataset, available at https://www.gloh2o.org. Satellite-based total cloud cover observations were obtained from the ESA Climate Change Initiative (ESA-CCI) Cloud dataset, available via the CEDA archive at https://catalogue.ceda.ac.uk/uuid/fb3750f5b2544403873f8788b3ed7817.

Top-of-atmosphere radiative fluxes and cloud radiative effect data were obtained from the CERES EBAF dataset, available at https://ceres.larc.nasa.gov/data/. Sea-ice concentration observations were obtained from the OSI SAF climate data record (OSI-450), available at https://osi-saf.eumetsat.int. Sea-ice thickness observations from the GIOMAS dataset were obtained from https://psc.apl.washington.edu/zhang/Global_seaice/data.html.

https://doi.org/10.5194/egusphere-2026-1289
Preprint. Discussion started: 21 May 2026

Acknowledgements

This work was supported by the EU funded EERIE project, which received funding from the European Union's Horizon Europe research and innovation programme under Grant Agreement No. 101081383. The simulations were performed using high-performance computing resources provided by the Jülich Supercomputing Centre (JSC) on the JUWELS system. Data storage, technical support, and data hosting were provided by the Deutsches Klimarechenzentrum (DKRZ), including dissemination via the World Data Center for Climate (WDCC). During the preparation of this manuscript, the authors used Paperpal and ChatGPT (OpenAI) to assist with language editing and to support the development of analysis code.

Author contributions

RG designed the study, performed the simulations and main analyses, prepared the simulation output, and wrote the manuscript. SKC contributed to the technical setup and HPC deployment of the kilometre-scale model configuration. NK performed the initial ocean only 5-year spinup. The overall structure and interpretation of the manuscript were developed together with TJ.

SBeyer provided the IFS–FESOM coupling and model schematic. AD contributed the ocean mean state analysis and corresponding figure. SBerzina produced the ocean mesoscale eddy radius diagnostics. SLibera contributed the sea-ice concentration analysis, and SLoza contributed the sea-ice thickness diagnostics. CW contributed the analysis of drift in the control simulations. NK contributed supplementary analyses of the long-term evolution of the historical simulation deep-ocean properties. PS developed the preliminary script to calculate AMOC on native NG5 grid. All authors contributed to the interpretation of the results.

Competing interests

Authors declare to competing interest for this work.

References

Adler, R. F., Sapiano, M. R. P., Huffman, G. J., Wang, J.-J., Gu, G., Bolvin, D., Chiu, L., Schneider, U., Becker, A., Nelkin, E., Xie, P., Ferraro, R., and Shin, D.-B.: The Global Precipitation Climatology Project (GPCP) Monthly Analysis (New Version 2.3) and a Review of 2017 Global Precipitation, Atmosphere, 9, 138, https://doi.org/10.3390/atmos9040138, 2018.

Aengenheyster, M., Roberts, C. D., Aguridan, R., Griffith, M., Hogan, R., Reuter, B., Roberts, M. J., Sarmany, D., Senan, R., Stockdale, T. N., Villaume, S., and Wachsmann, F.: Multi-decadal high-resolution historical simulations with the ECMWF 1 global atmosphere model, Sci. Data, Under review.

Beck, H. E., Wood, E. F., Pan, M., Fisher, C. K., Miralles, D. G., Dijk, A. I. J. M. van, McVicar, T. R., and Adler, R. F.: MSWEP V2 Global 3-Hourly 0.1° Precipitation: Methodology and Quantitative Assessment, Bull. Am. Meteorol. Soc., 100, 473–500, https://doi.org/10.1175/BAMS-D-17-0138.1, 2019.

Beech, N., Rackow, T., Semmler, T., and Jung, T.: Exploring the ocean mesoscale at reduced computational cost with FESOM 2.5: efficient modeling strategies applied to the Southern Ocean, Geosci. Model Dev., 17, 529–543, https://doi.org/10.5194/gmd-17-529-2024, 2024.

Beljaars, A. C. M., Brown, A. R., and Wood, N.: A new parametrization of turbulent orographic form drag, Q. J. R. Meteorol. Soc., 130, 1327–1347, https://doi.org/10.1256/qj.03.73, 2004.

https://doi.org/10.5194/egusphere-2026-1289
Preprint. Discussion started: 21 May 2026

1219 Bellucci, A., Athanasiadis, P. J., Scoccimarro, E., Ruggieri, P., Gualdi, S., Fedele, G., Haarsma, R.
1220 J., Garcia-Serrano, J., Castrillo, M., Putrahasan, D., Sanchez-Gomez, E., Moine, M.-P., Roberts,
1221 C. D., Roberts, M. J., Seddon, J., and Vidale, P. L.: Air-Sea interaction over the Gulf Stream in
1222 an ensemble of HighResMIP present climate simulations, Clim. Dyn., 56, 2093–2111,
1223 https://doi.org/10.1007/s00382-020-05573-z, 2021.

1224 Belušić, D. and Lind, P.: Benefits of km-scale climate modeling for winds in complex terrain:
1225 strong versus weak winds, https://doi.org/10.5194/egusphere-2025-1281, 28 March 2025.

1226 Bordoni, S., Kang, S. M., Shaw, T. A., Simpson, I. R., and Zanna, L.: The futures of climate
1227 modeling, Npj Clim. Atmospheric Sci., 8, 99, https://doi.org/10.1038/s41612-025-00955-8,
1228 2025.

1229 Boussetta, S., Balsamo, G., Arduini, G., Dutra, E., McNorton, J., Choulga, M., Agustí-Panareda,
1230 A., Beljaars, A., Wedi, N., Munõz-Sabater, J., de Rosnay, P., Sandu, I., Hadade, I., Carver, G.,
1231 Mazzetti, C., Prudhomme, C., Yamazaki, D., and Zsoter, E.: ECLand: The ECMWF Land Surface
1232 Modelling System, Atmosphere, 12, 723, https://doi.org/10.3390/atmos12060723, 2021.

1233 de Boyer Montégut, C.: Mixed layer depth climatology computed with a density threshold
1234 criterion of 0.03 kg/m3 from 10 m depth value, , https://doi.org/10.17882/91774, 2023.

1235 de Boyer Montégut, C., Madec, G., Fischer, A. S., Lazar, A., and Iudicone, D.: Mixed layer depth
1236 over the global ocean: An examination of profile data and a profile-based climatology, J.
1237 Geophys. Res. Oceans, 109, https://doi.org/10.1029/2004JC002378, 2004.

1238 Caldwell, P. M., Terai, C. R., Hillman, B., Keen, N. D., Bogenschutz, P., Lin, W., Beydoun, H.,
1239 Taylor, M., Bertagna, L., Bradley, A. M., Clevenger, T. C., Donahue, A. S., Eldred, C., Foucar, J.,
1240 Golaz, J.-C., Guba, O., Jacob, R., Johnson, J., Krishna, J., Liu, W., Pressel, K., Salinger, A. G., Singh,
1241 B., Steyer, A., Ullrich, P., Wu, D., Yuan, X., Shpund, J., Ma, H.-Y., and Zender, C. S.: Convection-
1242 Permitting Simulations With the E3SM Global Atmosphere Model, J. Adv. Model. Earth Syst.,
1243 13, e2021MS002544, https://doi.org/10.1029/2021MS002544, 2021.

1244 Caneill, R., Roquet, F., Madec, G., and Nycander, J.: The Polar Transition from Alpha to Beta
1245 Regions Set by a Surface Buoyancy Flux Inversion, J. Phys. Oceanogr., 52, 1887–1902,
1246 https://doi.org/10.1175/JPO-D-21-0295.1, 2022.

1247 Chang, P., Zhang, S., Danabasoglu, G., Yeager, S. G., Fu, H., Wang, H., Castruccio, F. S., Chen,
1248 Y., Edwards, J., Fu, D., Jia, Y., Laurindo, L. C., Liu, X., Rosenbloom, N., Small, R. J., Xu, G., Zeng,
1249 Y., Zhang, Q., Bacmeister, J., Bailey, D. A., Duan, X., DuVivier, A. K., Li, D., Li, Y., Neale, R.,
1250 Stössel, A., Wang, L., Zhuang, Y., Baker, A., Bates, S., Dennis, J., Diao, X., Gan, B., Gopal, A., Jia,
1251 D., Jing, Z., Ma, X., Saravanan, R., Strand, W. G., Tao, J., Yang, H., Wang, X., Wei, Z., and Wu, L.:
1252 An Unprecedented Set of High-Resolution Earth System Simulations for Understanding
1253 Multiscale Interactions in Climate Variability and Change, J. Adv. Model. Earth Syst., 12,
1254 e2020MS002298, https://doi.org/10.1029/2020MS002298, 2020.

1255 Chassignet, E. P. and Xu, X.: Impact of Horizontal Resolution (1/12° to 1/50°) on Gulf Stream
1256 Separation, Penetration, and Variability, J. Phys. Oceanogr., 47, 1999–2021,
1257 https://doi.org/10.1175/JPO-D-17-0031.1, 2017.

1258 Chassignet, E. P. and Xu, X.: On the Importance of High-Resolution in Large-Scale Ocean
1259 Models, Adv. Atmospheric Sci., 38, 1621–1634, https://doi.org/10.1007/s00376-021-0385-7,
1260 2021.

https://doi.org/10.5194/egusphere-2026-1289
Preprint. Discussion started: 21 May 2026

Chassignet, E. P., Yeager, S. G., Fox-Kemper, B., Bozec, A., Castruccio, F., Danabasoglu, G., Horvat, C., Kim, W. M., Koldunov, N., Li, Y., Lin, P., Liu, H., Sein, D. V., Sidorenko, D., Wang, Q., and Xu, X.: Impact of horizontal resolution on global ocean–sea ice model simulations based on the experimental protocols of the Ocean Model Intercomparison Project phase 2 (OMIP-2), Geosci. Model Dev., 13, 4595–4637, https://doi.org/10.5194/gmd-13-4595-2020, 2020.

Danilov, S., Sidorenko, D., Wang, Q., and Jung, T.: The Finite-volumE Sea ice–Ocean Model (FESOM2), Geosci. Model Dev., 10, 765–789, https://doi.org/10.5194/gmd-10-765-2017, 2017.

Delpech, A., Tréguier, A.-M., Marié, L., Ghosh, R., and Roberts, M. J.: Persistent Coastal Temperature Biases in km-Scale Climate Models Due To Unresolved Oceanic Tidal Mixing, Geophys. Res. Lett., 52, e2025GL118014, https://doi.org/10.1029/2025GL118014, 2025.

Demory, M.-E., Berthou, S., Fernández, J., Sørland, S. L., Brogli, R., Roberts, M. J., Beyerle, U., Seddon, J., Haarsma, R., Schär, C., Buonomo, E., Christensen, O. B., Ciarlo`, J. M., Fealy, R., Nikulin, G., Peano, D., Putrasahan, D., Roberts, C. D., Senan, R., Steger, C., Teichmann, C., and Vautard, R.: European daily precipitation according to EURO-CORDEX regional climate models (RCMs) and high-resolution global climate models (GCMs) from the High-Resolution Model Intercomparison Project (HighResMIP), Geosci. Model Dev., 13, 5485–5506, https://doi.org/10.5194/gmd-13-5485-2020, 2020.

Dijkstra, H. A.: The ENSO phenomenon: theory and mechanisms, in: Advances in Geosciences, 1st Alexander von Humboldt International Conference - 1st Alexander von Humboldt Conference, Guayaquil, Ecuador, 16–20 May 2005, 3–15, https://doi.org/10.5194/adgeo-6-3-2006, 2006.

Doblas-Reyes, F. J., Kontkanen, J., Sandu, I., Acosta, M., Al Turjmam, M. H., Alsina-Ferrer, I., Andrés-Martínez, M., Arriola, L., Axness, M., Batlle Martín, M., Bauer, P., Becker, T., Beltrán, D., Beyer, S., Bockelmann, H., Bretonnière, P.-A., Cabaniols, S., Caprioli, S., Castrillo, M., Chandrasekar, A., Cheedela, S., Correal, V., Danovaro, E., Davini, P., Enkovaara, J., Frauen, C., Früh, B., Gaya Àvila, A., Ghinassi, P., Ghosh, R., Ghosh, S., González, I., Grayson, K., Griffith, M., Hadade, I., Haine, C., Hartick, C., Haus, U.-U., Hearne, S., Järvinen, H., Jiménez, B., John, A., Juchem, M., Jung, T., Kegel, J., Kelbling, M., Keller, K., Kinoshita, B., Kiszler, T., Klocke, D., Kluft, L., Koldunov, N., Kölling, T., Kolstela, J., Kornblueh, L., Kosukhin, S., Lacima-Nadolnik, A., Leal Rojas, J. J., Lehtiranta, J., Lunttila, T., Luoma, A., Manninen, P., Medvedev, A., Milinski, S., Mohammed, A. O. A., Müller, S., Naryanappa, D., Nazarova, N., Niemelä, S., Niraula, B., Nortamo, H., Nummelin, A., Nurisso, M., Ortega, P., Paronuzzi, S., Pedruzo Bagazgoitia, X., Pelletier, C., Peña, C., Polade, S., Pradhan, H., Quintanilla, R., Quintino, T., Rackow, T., Räisänen, J., Rajput, M. M., Redler, R., Reuter, B., Rocha Monteiro, N., Roura-Adserias, F., Ruppert, S., Sayed, S., Schnur, R., Sharma, T., Sidorenko, D., Sievi-Korte, O., Soret, A., Steger, C., Stevens, B., Streffing, J., et al.: The Destination Earth digital twin for climate change adaptation, EGUsphere, 1–41, https://doi.org/10.5194/egusphere-2025-2198, 2025.

ECMWF: IFS Documentation CY48R1 - Part VII: ECMWF Wave Model, in: IFS Documentation, ECMWF, 2023.

Eyring, V., Gillett, N. P., Achuta Rao, K. M., Barimalala, R., Barreiro Parrillo, M., Bellouin, N., Cassou, C., Durack, P. J., Kosaka, Y., McGregor, S., Min, S., Morgenstern, O., and Sun, Y.: Human Influence on the Climate System, in: Climate Change 2021: The Physical Science Basis. Contribution of Working Group I to the Sixth Assessment Report of the Intergovernmental Panel on Climate Change, edited by: Masson-Delmotte, V., Zhai, P., Pirani, A., Connors, S. L., Péan, C., Berger, S., Caud, N., Chen, Y., Goldfarb, L., Gomis, M. I., Huang, M., Leitzell, K., Lonnoy,

https://doi.org/10.5194/egusphere-2026-1289
Preprint. Discussion started: 21 May 2026

E., Matthews, J. B. R., Maycock, T. K., Waterfield, T., Yelekçi, O., Yu, R., and Zhou, B., Cambridge University Press, Cambridge, United Kingdom and New York, NY, USA, 423–552, https://doi.org/10.1017/9781009157896.005, 2021.

Fox-Kemper, B., Adcroft, A., Böning, C. W., Chassignet, E. P., Curchitser, E., Danabasoglu, G., Eden, C., England, M. H., Gerdes, R., Greatbatch, R. J., Griffies, S. M., Hallberg, R. W., Hanert, E., Heimbach, P., Hewitt, H. T., Hill, C. N., Komuro, Y., Legg, S., Le Sommer, J., Masina, S., Marsland, S. J., Penny, S. G., Qiao, F., Ringler, T. D., Treguier, A. M., Tsujino, H., Uotila, P., and Yeager, S. G.: Challenges and Prospects in Ocean Circulation Models, Front. Mar. Sci., 6, https://doi.org/10.3389/fmars.2019.00065, 2019.

Fox-Kemper, B., Hewitt, H. T., Xiao, C., Adalgeirsdottir, G., Drijfhout, S. S., Edwards, T. L., Golledge, N. R., Hemer, M., Kopp, R. E., Krinner, G., Mix, A., Notz, D., Nowicki, S., Nurhati, I. S., Ruiz, L., Sallee, J.-B., Slangen, A. B. A., and Yu, Y.: Climate Change 2021: The Physical Science Basis, in: Contribution of Working Group I to the Sixth Assessment Report of the Intergovernmental Panel on Climate Change, edited by: Masson-Delmotte, V., Zhai, P., Pirani, A., Connors, S.-L., Péan, C., Berger, S., Caud, N., Chen, Y., Goldfarb, L., Gomis, M. I., Huang, M., Leitzell, K., Lonnoy, E., Matthews, J. B. R., Maycock, T. K., Waterfield, T., Yelekçi, O., Yu, R., and Zhou, B., Cambridge University Press, 1211–1362, https://doi.org/10.1017/9781009157896.011, 2021.

Gao, L., Bernhardt, M., and Schulz, K.: Elevation correction of ERA-Interim temperature data in complex terrain, Hydrol. Earth Syst. Sci., 16, 4661–4673, https://doi.org/10.5194/hess-16-4661-2012, 2012.

Good, S. A., Martin, M. J., and Rayner, N. A.: EN4: Quality controlled ocean temperature and salinity profiles and monthly objective analyses with uncertainty estimates, J. Geophys. Res. Oceans, 118, 6704–6716, https://doi.org/10.1002/2013JC009067, 2013.

Grist, J. P., Josey, S. A., Sinha, B., Catto, J. L., Roberts, M. J., and Coward, A. C.: Future Evolution of an Eddy Rich Ocean Associated with Enhanced East Atlantic Storminess in a Coupled Model Projection, Geophys. Res. Lett., 48, e2021GL092719, https://doi.org/10.1029/2021GL092719, 2021.

Guilyardi, E., Capotondi, A., Lengaigne, M., Thual, S., and Wittenberg, A. T.: ENSO Modeling, in: El Niño Southern Oscillation in a Changing Climate, American Geophysical Union (AGU), 199–226, https://doi.org/10.1002/9781119548164.ch9, 2020.

Haarsma, R. J., Roberts, M. J., Vidale, P. L., Senior, C. A., Bellucci, A., Bao, Q., Chang, P., Corti, S., Fučkar, N. S., Guemas, V., von Hardenberg, J., Hazeleger, W., Kodama, C., Koenigk, T., Leung, L. R., Lu, J., Luo, J.-J., Mao, J., Mizielinski, M. S., Mizuta, R., Nobre, P., Satoh, M., Scoccimarro, E., Semmler, T., Small, J., and von Storch, J.-S.: High Resolution Model Intercomparison Project (HighResMIP v1.0) for CMIP6, Geosci. Model Dev., 9, 4185–4208, https://doi.org/10.5194/gmd-9-4185-2016, 2016.

Hersbach, H., Bell, B., Berrisford, P., Hirahara, S., Horányi, A., Muñoz-Sabater, J., Nicolas, J., Peubey, C., Radu, R., Schepers, D., Simmons, A., Soci, C., Abdalla, S., Abellan, X., Balsamo, G., Bechtold, P., Biavati, G., Bidlot, J., Bonavita, M., De Chiara, G., Dahlgren, P., Dee, D., Diamantakis, M., Dragani, R., Flemming, J., Forbes, R., Fuentes, M., Geer, A., Haimberger, L., Healy, S., Hogan, R. J., Hólm, E., Janisková, M., Keeley, S., Laloyaux, P., Lopez, P., Lupu, C., Radnoti, G., de Rosnay, P., Rozum, I., Vamborg, F., Villaume, S., and Thépaut, J.-N.: The ERA5 global reanalysis, Q. J. R. Meteorol. Soc., 146, 1999–2049, https://doi.org/10.1002/qj.3803, 2020.

https://doi.org/10.5194/egusphere-2026-1289
Preprint. Discussion started: 21 May 2026

Hurrell, J. W., Kushnir, Y., Ottersen, G., and Visbeck, M.: An Overview of the North Atlantic Oscillation, in: The North Atlantic Oscillation: Climatic Significance and Environmental Impact, American Geophysical Union (AGU), 1–35, https://doi.org/10.1029/134GM01, 2003.

Jin, F.-F., Chen, H.-C., Zhao, S., Hayashi, M., Karamperidou, C., Stuecker, M. F., Xie, R., and Geng, L.: Simple ENSO Models, in: El Niño Southern Oscillation in a Changing Climate, American Geophysical Union (AGU), 119–151, https://doi.org/10.1002/9781119548164.ch6, 2020.

Kendon, E. J., Prein, A. F., Senior, C. A., and Stirling, A.: Challenges and outlook for convection-permitting climate modelling, Philos. Trans. R. Soc. Math. Phys. Eng. Sci., 379, 20190547, https://doi.org/10.1098/rsta.2019.0547, 2021.

Lavergne, T., Sørensen, A. M., Kern, S., Tonboe, R., Notz, D., Aaboe, S., Bell, L., Dybkjær, G., Eastwood, S., Gabarro, C., Heygster, G., Killie, M. A., Brandt Kreiner, M., Lavelle, J., Saldo, R., Sandven, S., and Pedersen, L. T.: Version 2 of the EUMETSAT OSI SAF and ESA CCI sea-ice concentration climate data records, The Cryosphere, 13, 49–78, https://doi.org/10.5194/tc-13-49-2019, 2019.

Leutwyler, D., Fuhrer, O., Lapillonne, X., Lüthi, D., and Schär, C.: Towards European-scale convection-resolving climate simulations with GPUs: a study with COSMO 4.19, Geosci. Model Dev., 9, 3393–3412, https://doi.org/10.5194/gmd-9-3393-2016, 2016.

Li, L., Bisht, G., Hao, D., and Leung, L. R.: Global 1 km land surface parameters for kilometer-scale Earth system modeling, Earth Syst. Sci. Data, 16, 2007–2032, https://doi.org/10.5194/essd-16-2007-2024, 2024.

Liu, Y. and Zhang, J.: Conductive Heat Flux Over Arctic Sea Ice From 1979 to 2022, J. Geophys. Res. Oceans, 130, e2024JC022062, https://doi.org/10.1029/2024JC022062, 2025.

Liu, Y., Cheng, L., Pan, Y., Tan, Z., Abraham, J., Zhang, B., Zhu, J., and Song, J.: How Well Do CMIP6 and CMIP5 Models Simulate the Climatological Seasonal Variations in Ocean Salinity?, Adv. Atmospheric Sci., 39, 1650–1672, https://doi.org/10.1007/s00376-022-1381-2, 2022.

Lott, F. and Miller, M. J.: A new subgrid-scale orographic drag parametrization: Its formulation and testing, Q. J. R. Meteorol. Soc., 123, 101–127, https://doi.org/10.1002/qj.49712353704, 1997.

Maykut, G. A.: The Surface Heat and Mass Balance, in: The Geophysics of Sea Ice, edited by: Untersteiner, N., Springer US, Boston, MA, 395–463, https://doi.org/10.1007/978-1-4899-5352-0_6, 1986.

Merchant, C. J., Embury, O., Bulgin, C. E., Block, T., Corlett, G. K., Fiedler, E., Good, S. A., Mittaz, J., Rayner, N. A., Berry, D., Eastwood, S., Taylor, M., Tsushima, Y., Waterfall, A., Wilson, R., and Donlon, C.: Satellite-based time-series of sea-surface temperature since 1981 for climate applications, Sci. Data, 6, 223, https://doi.org/10.1038/s41597-019-0236-x, 2019.

Mezzina, B., Roberts, C. D., Aengenheyster, M., Ghosh, R., Roberts, M. J., and Batlle Martin, M.: ENSO teleconnections in eddy-rich climate models, EGUsphere, 1–27, https://doi.org/10.5194/egusphere-2026-547, 2026.

Moon, J.-Y., Streffing, J., Lee, S.-S., Semmler, T., Andrés-Martínez, M., Chen, J., Cho, E.-B., Chu, J.-E., Franzke, C. L. E., Gärtner, J. P., Ghosh, R., Hegewald, J., Hong, S., Kim, D.-W., Koldunov, N., Lee, J.-Y., Lin, Z., Liu, C., Loza, S. N., Park, W., Roh, W., Sein, D. V., Sharma, S., Sidorenko, D.,

https://doi.org/10.5194/egusphere-2026-1289
Preprint. Discussion started: 21 May 2026

Son, J.-H., Stuecker, M. F., Wang, Q., Yi, G., Zapponini, M., Jung, T., and Timmermann, A.: Earth's future climate and its variability simulated at 9 km global resolution, Earth Syst. Dyn., 16, 1103–1134, https://doi.org/10.5194/esd-16-1103-2025, 2025.

Moreno-Chamarro, E., Caron, L.-P., Ortega, P., Loosveldt Tomas, S., and Roberts, M. J.: Can we trust CMIP5/6 future projections of European winter precipitation?, Environ. Res. Lett., 16, 054063, https://doi.org/10.1088/1748-9326/abf28a, 2021.

Moreno-Chamarro, E., Caron, L.-P., Loosveldt Tomas, S., Vegas-Regidor, J., Gutjahr, O., Moine, M.-P., Putrasahan, D., Roberts, C. D., Roberts, M. J., Senan, R., Terray, L., Tourigny, E., and Vidale, P. L.: Impact of increased resolution on long-standing biases in HighResMIP-PRIMAVERA climate models, Geosci. Model Dev., 15, 269–289, https://doi.org/10.5194/gmd-15-269-2022, 2022.

Orr, A., Bechtold, P., Scinocca, J., Ern, M., and Janiskova, M.: Improved Middle Atmosphere Climate and Forecasts in the ECMWF Model through a Nonorographic Gravity Wave Drag Parameterization, J. Clim., 23, 5905–5926, https://doi.org/10.1175/2010JCLI3490.1, 2010.

Planton, Y. Y., Guilyardi, E., Wittenberg, A. T., Lee, J., Gleckler, P. J., Bayr, T., McGregor, S., McPhaden, M. J., Power, S., Roehrig, R., Vialard, J., and Voldoire, A.: Evaluating Climate Models with the CLIVAR 2020 ENSO Metrics Package, Bull. Am. Meteorol. Soc., 102, E193–E217, https://doi.org/10.1175/BAMS-D-19-0337.1, 2021.

Platnick , S., Ackerman, S., King, M., and et.al.: MODIS Atmosphere L2 Cloud Product (06_L2), https://doi.org/10.5067/MODIS/MOD06_L2.006, 2015.

Rackow, T., Hegewald, J., Koldunov, N. V., Mogensen, K., Scholz, P., Sidorenko, D., and Streffing, J.: FESOM2.5 source code used in nextGEMS Cycle 3 simulations with IFS-FESOM, , https://doi.org/10.5281/ZENODO.10225419, 2023.

Rackow, T., Pedruzo-Bagazgoitia, X., Becker, T., Milinski, S., Sandu, I., Aguridan, R., Bechtold, P., Beyer, S., Bidlot, J., Boussetta, S., Deconinck, W., Diamantakis, M., Dueben, P., Dutra, E., Forbes, R., Ghosh, R., Goessling, H. F., Hadade, I., Hegewald, J., Jung, T., Keeley, S., Kluft, L., Koldunov, N., Koldunov, A., Kölling, T., Kousal, J., Kühnlein, C., Maciel, P., Mogensen, K., Quintino, T., Polichtchouk, I., Reuter, B., Sármány, D., Scholz, P., Sidorenko, D., Streffing, J., Sützl, B., Takasuka, D., Tietsche, S., Valentini, M., Vannière, B., Wedi, N., Zampieri, L., and Ziemen, F.: Multi-year simulations at kilometre scale with the Integrated Forecasting System coupled to FESOM2.5 and NEMOv3.4, Geosci. Model Dev., 18, 33–69, https://doi.org/10.5194/gmd-18-33-2025, 2025.

Reichler, T. and Kim, J.: How Well Do Coupled Models Simulate Today's Climate?, Bull. Am. Meteorol. Soc., 89, 303–312, https://doi.org/10.1175/BAMS-89-3-303, 2008.

Remedio, A. R., Teichmann, C., Buntemeyer, L., Sieck, K., Weber, T., Rechid, D., Hoffmann, P., Nam, C., Kotova, L., and Jacob, D.: Evaluation of New CORDEX Simulations Using an Updated Köppen–Trewartha Climate Classification, Atmosphere, 10, https://doi.org/10.3390/atmos10110726, 2019.

Richter, I. and Mechoso, C. R.: Orographic Influences on Subtropical Stratocumulus, J. Atmospheric Sci., 63, 2585–2601, https://doi.org/10.1175/JAS3756.1, 2006.

Roberts, C. D., Senan, R., Molteni, F., Boussetta, S., Mayer, M., and Keeley, S. P. E.: Climate model configurations of the ECMWF Integrated Forecasting System (ECMWF-IFS cycle 43r1)

https://doi.org/10.5194/egusphere-2026-1289
Preprint. Discussion started: 21 May 2026

for HighResMIP, Geosci. Model Dev., 11, 3681–3712, https://doi.org/10.5194/gmd-11-3681-2018, 2018.

Roberts, M. J., Baker, A., Blockley, E. W., Calvert, D., Coward, A., Hewitt, H. T., Jackson, L. C., Kuhlbrodt, T., Mathiot, P., Roberts, C. D., Schiemann, R., Seddon, J., Vannière, B., and Vidale, P. L.: Description of the resolution hierarchy of the global coupled HadGEM3-GC3.1 model as used in CMIP6 HighResMIP experiments, Geosci. Model Dev., 12, 4999–5028, https://doi.org/10.5194/gmd-12-4999-2019, 2019.

Roberts, M. J., Camp, J., Seddon, J., Vidale, P. L., Hodges, K., Vanniere, B., Mecking, J., Haarsma, R., Bellucci, A., Scoccimarro, E., Caron, L.-P., Chauvin, F., Terray, L., Valcke, S., Moine, M.-P., Putrasahan, D., Roberts, C., Senan, R., Zarzycki, C., and Ullrich, P.: Impact of Model Resolution on Tropical Cyclone Simulation Using the HighResMIP–PRIMAVERA Multimodel Ensemble, J. Clim., 33, 2557–2583, https://doi.org/10.1175/JCLI-D-19-0639.1, 2020a.

Roberts, M. J., Jackson, L. C., Roberts, C. D., Meccia, V., Docquier, D., Koenigk, T., Ortega, P., Moreno-Chamarro, E., Bellucci, A., Coward, A., Drijfhout, S., Exarchou, E., Gutjahr, O., Hewitt, H., Iovino, D., Lohmann, K., Putrasahan, D., Schiemann, R., Seddon, J., Terray, L., Xu, X., Zhang, Q., Chang, P., Yeager, S. G., Castruccio, F. S., Zhang, S., and Wu, L.: Sensitivity of the Atlantic Meridional Overturning Circulation to Model Resolution in CMIP6 HighResMIP Simulations and Implications for Future Changes, J. Adv. Model. Earth Syst., 12, e2019MS002014, https://doi.org/10.1029/2019MS002014, 2020b.

Roberts, M. J., Reed, K. A., Bao, Q., Barsugli, J. J., Camargo, S. J., Caron, L.-P., Chang, P., Chen, C.-T., Christensen, H. M., Danabasoglu, G., Frenger, I., Fučkar, N. S., Hasson, S. U., Hewitt, H. T., Huang, H., Kim, D., Kodama, C., Lai, M., Leung, L.-Y. R., Mizuta, R., Nobre, P., Ortega, P., Paquin, D., Roberts, C. D., Scoccimarro, E., Seddon, J., Treguier, A. M., Tu, C.-Y., Ullrich, P. A., Vidale, P. L., Wehner, M. F., Zarzycki, C. M., Zhang, B., Zhang, W., and Zhao, M.: High Resolution Model Intercomparison Project phase 2 (HighResMIP2) towards CMIP7, https://doi.org/10.5194/egusphere-2024-2582, 27 August 2024.

Sauvage, C., Lebeaupin Brossier, C., and Bouin, M.-N.: Towards kilometer-scale ocean–atmosphere–wave coupled forecast: a case study on a Mediterranean heavy precipitation event, Atmospheric Chem. Phys., 21, 11857–11887, https://doi.org/10.5194/acp-21-11857-2021, 2021.

Schär, C., Fuhrer, O., Arteaga, A., Ban, N., Charpilloz, C., Girolamo, S. D., Hentgen, L., Hoefler, T., Lapillonne, X., Leutwyler, D., Osterried, K., Panosetti, D., Rüdisühli, S., Schlemmer, L., Schulthess, T. C., Sprenger, M., Ubbiali, S., and Wernli, H.: Kilometer-Scale Climate Models: Prospects and Challenges, Bull. Am. Meteorol. Soc., 101, E567–E587, https://doi.org/10.1175/BAMS-D-18-0167.1, 2020.

Scholz, P., Sidorenko, D., Gurses, O., Danilov, S., Koldunov, N., Wang, Q., Sein, D., Smolentseva, M., Rakowsky, N., and Jung, T.: Assessment of the Finite-volumE Sea ice-Ocean Model (FESOM2.0) – Part 1: Description of selected key model elements and comparison to its predecessor version, Geosci. Model Dev., 12, 4875–4899, https://doi.org/10.5194/gmd-12-4875-2019, 2019.

Scoccimarro, E., Peano, D., Gualdi, S., Bellucci, A., Lovato, T., Fogli, P. G., and Navarra, A.: Extreme events representation in CMCC-CM2 standard and high-resolution general circulation models, Geosci. Model Dev., 15, 1841–1854, https://doi.org/10.5194/gmd-15-1841-2022, 2022.

https://doi.org/10.5194/egusphere-2026-1289
Preprint. Discussion started: 21 May 2026

Segura, H., Pedruzo-Bagazgoitia, X., Weiss, P., Müller, S. K., Rackow, T., Lee, J., Dolores-Tesillos, E., Benedict, I., Aengenheyster, M., Aguridan, R., Arduini, G., Baker, A. J., Bao, J., Bastin, S., Baulenas, E., Becker, T., Beyer, S., Bockelmann, H., Brüggemann, N., Brunner, L., Cheedela, S. K., Das, S., Denissen, J., Dragaud, I., Dziekan, P., Ekblom, M., Engels, J. F., Esch, M., Forbes, R., Frauen, C., Freischem, L., García-Maroto, D., Geier, P., Gierz, P., González-Cervera, Á., Grayson, K., Griffith, M., Gutjahr, O., Haak, H., Hadade, I., Haslehner, K., ul Hasson, S., Hegewald, J., Kluft, L., Koldunov, A., Koldunov, N., Kölling, T., Koseki, S., Kosukhin, S., Kousal, J., Kuma, P., Kumar, A. U., Li, R., Maury, N., Meindl, M., Milinski, S., Mogensen, K., Niraula, B., Nowak, J., Praturi, D. S., Proske, U., Putrasahan, D., Redler, R., Santuy, D., Sármány, D., Schnur, R., Scholz, P., Sidorenko, D., Spät, D., Sützl, B., Takasuka, D., Tompkins, A., Uribe, A., Valentini, M., Veerman, M., Voigt, A., Warnau, S., Wachsmann, F., Wacławczyk, M., Wedi, N., Wieners, K.-H., Wille, J., Winkler, M., Wu, Y., Ziemen, F., Zimmermann, J., Bender, F. A.-M., Bojovic, D., Bony, S., Bordoni, S., Brehmer, P., Dengler, M., Dutra, E., Faye, S., Fischer, E., van Heerwaarden, C., Hohenegger, C., Järvinen, H., Jochum, M., et al.: nextGEMS: entering the era of kilometer-scale Earth system modeling, EGUsphere, 1–39, https://doi.org/10.5194/egusphere-2025-509, 2025.

Shi, H., Jin, F.-F., Wills, R. C. J., Jacox, M. G., Amaya, D. J., Black, B. A., Rykaczewski, R. R., Bograd, S. J., García-Reyes, M., and Sydeman, W. J.: Global decline in ocean memory over the 21st century, Sci. Adv., 8, eabm3468, https://doi.org/10.1126/sciadv.abm3468, 2022.

Small, R. J., Kurian, J., Chang, P., Xu, G., Tsujino, H., Yeager, S., Danabasoglu, G., Kim, W. M., Altuntas, A., and Castruccio, F.: Eastern Boundary Upwelling Systems in Ocean–Sea Ice Simulations Forced by CORE and JRA55-do: Mean State and Variability at the Surface, J. Clim., 37, 2821–2848, https://doi.org/10.1175/JCLI-D-23-0511.1, 2024.

Stengel, M., Stapelberg, S., Sus, O., Finkensieper, S., Würzler, B., Philipp, D., Hollmann, R., Poulsen, C., Christensen, M., and McGarragh, G.: Cloud_cci Advanced Very High Resolution Radiometer post meridiem (AVHRR-PM) dataset version 3: 35-year climatology of global cloud and radiation properties, Earth Syst. Sci. Data, 12, 41–60, https://doi.org/10.5194/essd-12-41-2020, 2020.

Storto, A., Masina, S., and Navarra, A.: Evaluation of the CMCC eddy-permitting global ocean physical reanalysis system (C-GLORS, 1982–2012) and its assimilation components, Q. J. R. Meteorol. Soc., 142, 738–758, https://doi.org/10.1002/qj.2673, 2016.

Streffing, J., Sidorenko, D., Semmler, T., Zampieri, L., Scholz, P., Andrés-Martínez, M., Koldunov, N., Rackow, T., Kjellsson, J., Goessling, H., Athanase, M., Wang, Q., Hegewald, J., Sein, D. V., Mu, L., Fladrich, U., Barbi, D., Gierz, P., Danilov, S., Juricke, S., Lohmann, G., and Jung, T.: AWI-CM3 coupled climate model: description and evaluation experiments for a prototype post-CMIP6 model, Geosci. Model Dev., 15, 6399–6427, https://doi.org/10.5194/gmd-15-6399-2022, 2022.

Tiedtke, M.: A Comprehensive Mass Flux Scheme for Cumulus Parameterization in Large-Scale Models, Mon. Weather Rev., 117, 1779–1800, https://doi.org/10.1175/1520-0493(1989)117%3C1779:ACMFSF%3E2.0.CO;2, 1989.

Tiedtke, M.: Representation of Clouds in Large-Scale Models, Mon. Weather Rev., 121, 3040–3061, https://doi.org/10.1175/1520-0493(1993)121%3C3040:ROCILS%3E2.0.CO;2, 1993.

Untch, A. and Hortal, M.: A finite-element scheme for the vertical discretization of the semi-Lagrangian version of the ECMWF forecast model, Q. J. R. Meteorol. Soc., 130, 1505–1530, https://doi.org/10.1256/qj.03.173, 2004.

https://doi.org/10.5194/egusphere-2026-1289
Preprint. Discussion started: 21 May 2026

Vannière, B., Roberts, M., Vidale, P. L., Hodges, K., Demory, M.-E., Caron, L.-P., Scoccimarro, E., Terray, L., and Senan, R.: The Moisture Budget of Tropical Cyclones in HighResMIP Models: Large-Scale Environmental Balance and Sensitivity to Horizontal Resolution, J. Clim., 33, 8457–8474, https://doi.org/10.1175/JCLI-D-19-0999.1, 2020.

Vivoda, J., Smolíková, P., and Simarro, J.: Finite Elements Used in the Vertical Discretization of the Fully Compressible Core of the ALADIN System, Mon. Weather Rev., 146, 3293–3310, https://doi.org/10.1175/MWR-D-18-0043.1, 2018.

Wang, Q., Koldunov, N. V., Danilov, S., Sidorenko, D., Wekerle, C., Scholz, P., Bashmachnikov, I. L., and Jung, T.: Eddy Kinetic Energy in the Arctic Ocean From a Global Simulation With a 1-km Arctic, Geophys. Res. Lett., 47, e2020GL088550, https://doi.org/10.1029/2020GL088550, 2020.

Wedi, N., Sandu, I., Bauer, P., Acosta, M., Andersen, R. C., Andrae, U., Auger, L., Balsamo, G., Baousis, V., Bennett, V., Bennett, A., Buontempo, C., Bretonnière, P.-A., Capell, R., Castrillo, M., Chantry, M., Chevallier, M., Correa, R., Davini, P., Denby, L., Doblas-Reyes, F., Dueben, P., Fischer, C., Frauen, C., Frogner, I.-L., Früh, B., Gascón, E., Gérard, E., Gorwits, O., Geenen, T., Grayson, K., Guenova-Rubio, N., Hadade, I., von Hardenberg, J., Haus, U.-U., Hawkes, J., Hirtl, M., Hoffmann, J., Horvath, K., Järvinen, H., Jung, T., Kann, A., Klocke, D., Koldunov, N., Kontkanen, J., Sievi-Korte, O., Kristiansen, J., Kuwertz, E., Mäkelä, J., Maljutenko, I., Manninen, P., McKnight, U. S., Milinski, S., Mueller, A., McNally, A., Modigliani, U., Narayanappa, D., Nielsen, K. P., Nipen, T., Nortamo, H., Peuch, V.-H., Polade, S., Quintino, T., Schicker, I., Reuter, B., Smart, S., Sleigh, M., Suttie, M., Termonia, P., Thober, S., Randriamampianina, R., Theeuwes, N., Thiemert, D., Vannière, B., Vannitsem, S., Wittmann, C., Yang, X., Pontaud, M., Stevens, B., and Pappenberger, F.: Implementing digital twin technology of the earth system in Destination Earth, J. Eur. Meteorol. Soc., 3, 100015, https://doi.org/10.1016/j.jemets.2025.100015, 2025.

Wielicki, B. A., Barkstrom, B. R., Harrison, E. F., Lee, R. B., Smith, G. L., and Cooper, J. E.: Clouds and the Earth's Radiant Energy System (CERES): An Earth Observing System Experiment, Bull. Am. Meteorol. Soc., 77, 853–868, https://doi.org/10.1175/1520-0477(1996)077%3C0853:CATERE%3E2.0.CO;2, 1996.

Yang, H. and Zhu, J.: Equilibrium thermal response timescale of global oceans, Geophys. Res. Lett., 38, https://doi.org/10.1029/2011GL048076, 2011.

Yeager, S. G., Chang, P., Danabasoglu, G., Rosenbloom, N., Zhang, Q., Castruccio, F. S., Gopal, A., Cameron Rencurrel, M., and Simpson, I. R.: Reduced Southern Ocean warming enhances global skill and signal-to-noise in an eddy-resolving decadal prediction system, Npj Clim. Atmospheric Sci., 6, 1–13, https://doi.org/10.1038/s41612-023-00434-y, 2023.

Zhang, J. and Rothrock, D. A.: Modeling Global Sea Ice with a Thickness and Enthalpy Distribution Model in Generalized Curvilinear Coordinates, Mon. Weather Rev., 131, 845–861, https://doi.org/10.1175/1520-0493(2003)131%3C0845:MGSIWA%3E2.0.CO;2, 2003.